RESEARCH ARTICLE

VOLCANICA

Lower crustal magmatic processes and andesite genesis at Shiveluch Volcano

Andrea E. Goltz *α,β and Michael J. Krawczynski β

α Earth and Planets Laboratory, Carnegie Institution for Science, Washington, DC, USA.
β Department of Earth, Environmental, and Planetary Science, Washington University in St. Louis, St. Louis, MO, USA.

Submitted: 2025-06-11 | Accepted: 2026-07-01 | Published: 2026-07-02

Editor: M. Mangler | Production: A. Ryan

Abstract

The silicic melts that eventually erupt at arc volcanoes are cumulative products of crystallization and assimilation in the upper and lower crust. Yet, the storage conditions of magma in the lower crust are less well constrained than in the upper crust. In this study, we conduct and analyze hydrous piston cylinder experiments to determine the mid-to-lower crustal magma storage conditions of primitive melt at Shiveluch, an arc volcano located in northern Kamchatka. The near-liquidus assemblage of amphibole and olivine, observed in mafic enclaves, empirically compared to experimental products requires storage of primitive magmas at pressures between 500 MPa and 1 GPa, temperatures from 1000–1100 °C, and high (≥ 7.2 wt.%) H_2O contents. Compositions of glasses in our experiments also show that crystallization-driven differentiation in the lower crust cannot be the only process involved in the production of andesites at Shiveluch. By comparing synthetic and natural compositions of amphibole we determine that anatexis of the lower crust is also likely to significantly contribute to produce andesitic melts at Shiveluch.

Keywords: Arc volcanism; Subduction zone; Crystallization; Experimental petrology; Crustal melting; Hydrous magma.

1 Introduction

The lower crust sets the stage for upper crustal magmatic processes and eruptions at arc volcanoes. Continued addition of hot, primitive magma from the mantle to the bottommost crust establishes a lower crustal "hot zone" where magmas evolve [e.g. Annen et al. 2006]. Fractional crystallization of olivine, pyroxenes, feldspar, Fe-Ti oxides, and amphibole from primitive magmas in the lower crust can produce the relatively silicic melts that are stored and partially crystallized in the upper crust [e.g. Sisson et al. 2005; Blatter et al. 2013; Nandedkar et al. 2014; Blatter et al. 2017; Ulmer et al. 2018]. Melting of surrounding lower crustal rocks can also produce intermediate to silicic melts in greatere.g. volumes than fractional crystallization per unit mantle-derived basalt [e.g. Till et al. 2019]. Some combination of both processes produces the silicic magmas that erupt at arc volcanoes.

Despite the importance of the lower crust to the transcrustal magma system, pressures and temperatures of magma storage are more commonly estimated for silicic magmas in the upper crust (see, for example, the overwhelmingly shallow storage depths compiled for Cascades volcanoes by Wieser et al. [2023]). Storage conditions provide quantitative constraints on conceptual models of crustal structure. They can be directly compared to the depths of earthquakes to relate chemical processes to earthquakes [e.g. Dayton et al. 2023] or compared to other geophysical constraints on the current depths of magma storage (as done in Wieser et al. [2023]). Storage conditions of magmas in the upper crust have been assessed by application of `rhyolite-MELTS` [e.g. Gualda et al. 2012; Pamukcu et al. 2015; Harmon et al. 2024], empirically calibrated mineral and melt thermobarometers [e.g. Putirka 2008; Wieser et al. 2022], analysis of volatiles in melt inclusions [e.g. Barth et al. 2024], and experimental determination of phase diagrams [e.g. Rutherford and Devine 1996; Hammer et al. 2002; Pichavant et al. 2002]. Several factors render the conditions of lower crustal magma storage challenging to estimate. For one, the signatures of lower crustal processes can be difficult to isolate from the signatures of upper crustal processes in erupted silicic magmas because they may be mixed away or because they are overprinted by diffusive re-equilibration. Moreover, the stability of amphibole—hypothesized to crystallize in lower crustal zones [e.g. Davidson et al. 2013]—cannot be predicted by `rhyolite-MELTS`, which inhibits its use in this scenario. These challenges limit the assessment of lower crustal magma storage conditions.

In this study, we take an experimental approach to determine the mid-to-lower crustal magma storage conditions of primitive melt at Shiveluch, an arc volcano located in northern Kamchatka. Shiveluch has had more VEI 4+ eruptions in the Holocene than any other volcano [Global Volcanism Program 2025], and thus it is particularly consequential to understand the magmatic processes occurring beneath it. The compositions of a basalt and basaltic andesite hypothesized to reflect the compositions of magmas feeding the Shiveluch crustal plumbing system are preserved in two tephra units [Volynets et al. 1997; Ponomareva et al. 2007].

In their study of mafic enclaves from Shiveluch, Goltz et al. [2020] identified a likely near-liquidus phase assemblage of amphibole, olivine, and clinopyroxene. The mafic enclaves are basaltic to basaltic andesitic blebs of magma sampled from within an andesitic host rock at Shiveluch. The enclaves are distinct from the two tephra units described above but are hypothesized to be related via fractional crystallization [Goltz et al. 2020]. The enclaves' crenulate margins at the contact with the andesite suggest that they were still at least partially molten upon contact with the andesite. Models vary on how mafic enclaves are formed and preserved [e.g. Ruprecht et al. 2020], although, in general, they are taken as evidence of mingling

* agoltz@carnegiescience.edu

between mafic and felsic magmas in the upper crust (i.e. as a result of mafic recharge or rejuvenation; Bacon [1986]). The enclaves reflect the composition of more primitive magmas associated with the Shiveluch system. Some enclaves contain very high Mg# (i.e. Fo > 88) olivine, demonstrating that the enclaves preserve the mineral record of near-liquidus crystallization. Many enclaves contain amphibole and plagioclase that is complexly zoned, suggesting a protracted history of mixing and rejuvenation, potentially within the mid to lower crust; this line of evidence leads us to interpret the enclaves as representing a lower crustal, mushy "hot zone" [Annen et al. 2006].

Using mineral thermometry and hygrometry, Goltz et al. [2020] showed that magmas with water contents of at least 10 wt.% were stored in the lower crust at ~1060 °C and at a minimum of approximately 16 km depth (~460 MPa). The goal of this study is to experimentally reproduce the mineral assemblage found in these enclaves (i.e. olivine + amphibole ± clinopyroxene) to assess the lower crustal storage and differentiation conditions of Shiveluch mafic melts, with particular focus on the major and minor element chemistry of experimental amphibole. Here, we experimentally constrain the phase relations of the two different Shiveluch primitive magma compositions, hypothesized to be parental to erupted Shiveluch enclaves and andesites, at a range of water contents and temperatures at mid-to-lower crustal pressures (500 MPa and 1 GPa). The resulting experimental co-existing crystal assemblages, phase compositions, and stability are used to isolate pressures, temperatures, and water contents at which the near-liquidus assemblage of amphibole, olivine, and clinopyroxene is stable and, thus, determine the likely pressures and temperatures of primitive magmatic storage. Additionally, using the chemistry of synthetic glass and amphibole, we constrain the processes involved in producing intermediate magmas at Shiveluch.

2 Methods

2.1 Starting material synthesis and capsule Fe-saturation

Phase equilibrium crystallization experiments were conducted on starting compositions representative of the major element composition of tephra erupted at Shiveluch 3959 BP and 8363 BP [e.g. Ponomareva et al. 2015], or related to these compositions by fractional crystallization or olivine addition (Table 1). In total, eight synthetic mixes were used in this study, and their compositions (confirmed by and with uncertainties based on repeated electron probe microanalysis of glassed mixes; see Supplementary Material [Goltz 2026] for more information on mix preparation for these analyses and potential sources of heterogeneity) are reported in Table 1. The eight mixes are related to one of two tephra compositions proposed to represent the parental composition of magmas at Shiveluch [e.g. Volynets et al. 1997; Goltz et al. 2020]. The 3959 BP tephra major element composition is more magnesian and potassic than the 8363 BP tephra; thus, throughout this study, experiments done on mixes related to the 3959 BP tephra composition will be referred to as "hi-K" and experiments conducted on mixes related to the 8363 BP tephra composition will be referred to as "lo-K". Instead of considering the phase relations resulting from experiments on each mix, in this study, we group experimental results by the tephra to which the mix is related because they are a part of the same chemical system. By conducting experiments on the tephra compositions and their evolved derivatives, we seek to partially simulate the effects of equilibrium and fractional crystallization on phase equilibria and chemistry.

We experimented on three mixes related to the hi-K tephra: two modeled after the tephra composition itself (from Ponomareva et al. [2007]; mix 60 and mix 70, where mix 60 was decarbonated and mix 70 was not) and one mix representing a composition where olivine was added incrementally to bring the tephra composition into equilibrium with Fo_{92} olivine (composition from Gavrilenko et al. [2016]; mix 53, which we term the hi-K tephra parent and which was decarbonated). For the lo-K tephra, we conducted experiments on five starting mixes with three overall target compositions: two mixes modeled on the tephra composition (from Ponomareva et al. [2007]; mix 59 and mix 73, where mix 73 was not decarbonated), one mix modeled after a composition where olivine was iteratively added to bring the tephra into equilibrium with Fo_{92} olivine (assuming an Fe-Mg K_D of 0.3; mix 54, which we term the lo-K tephra parent and which was decarbonated), and two mixes modeled after the glass composition from experiment OD161 (Table 2), where Na_2O and K_2O were corrected for alkali loss to a fluid (as discussed further below) using the batch crystallization equation, mineral-melt partition coefficients of Na and K for pyroxene and olivine, the calculated proportions of pyroxene and olivine from mass balance, melt composition as analyzed by EPMA, and a melt fraction of 81 % (slightly different than our reported value of 83 % because it used an earlier version of the LIME algorithm; mixes 76 and 79, where mix 79 was not decarbonated).

A subset of these experiments (F136, OD102, F163, F174, OD143, F137, OD109, and OD144; Table 2) were previously published in Goltz et al. [2022]. The phase proportions of these experiments have been recalculated using the updated algorithm LIME as published in Prissel et al. [2023] and some are slightly different than those reported in Goltz et al. [2022]. The phase proportions—and particularly their uncertainties (reported in Table 3 and Tables S1, S2, and S3 of the Supplementary Material [Goltz 2026])—as published in this study are more robust and supersede the calculated phase proportions from Goltz et al. [2022].

Experiments were run water saturated, water undersaturated with no added CO_2, or water undersaturated with mixed volatiles (i.e. H_2O and CO_2). Non-mixed volatile experiments were prepared by dehydrating and decarbonating starting mixes and adding free water to the starting mix during capsule preparation, whereas mixed volatile experiments were conducted on mixes with added gibbsite and which were not decarbonated. Mixed volatile experiments had molar H_2O/CO_2 ranging from 2.30–2.77 and X_{H_2O}(defined as H_2O / (H_2O + CO_2), all in moles) of 0.70–0.73 (Table 1). Mixes were synthesized using a combination of SiO_2, TiO_2, Al_2O_3, $Al(OH)_3$ (mixed volatile mixes only), MnO, MgO, $Mg(OH)_2$, $CaSiO_3$, Na_2CO_3, K_2CO_3, $AlPO_4$, FeO, Fe_2O_3, and Fe_0. Mass balance

9(2): 455–479. https://doi.org/10.30909/vol.1jow6351

Table 1: Average compositions of experimental starting materials from repeated electron microprobe analysis and natural tephras from Ponomareva et al. [2007] in oxide wt.%. σ is the 1 standard deviation of the number of analyses. X_{H_2O} and H_2O / CO_2 are calculated from quantity of carbonates, and hydroxides added to starting mixture in moles. H_2O in wt.% is calculated from the quantity of hydroxides added to the starting mixture when all volatile and major elements are normalized to 100.

Mix no. and Description	53-hiK Tephra Parent		60-hiK Tephra		70-Mixed Volatile hiK Tephra		54-loK Tephra Parent		59-loK Tephra		73-Mixed Volatile loK Tephra		76-Evolved loK Tephra		79-Mixed Volatile Evolved loK Tephra		hiK (3959 BP)	loK (8363 BP)
No. Analyses	10		38		5		16		51		18		10		9		Tephra[a]	Tephra[a]
	avg	σ	avg	σ	avg	σ	avg	σ	avg	σ	avg	σ	avg	σ	avg	σ		
SiO_2	52.80	0.83	52.54	0.39	55.13	0.84	52.10	0.27	54.02	1.01	55.62	0.71	55.03	1.84	57.36	1.85	52.32	54.12
TiO_2	0.77	0.04	0.81	0.03	0.79	0.02	0.62	0.03	0.75	0.04	0.76	0.04	0.73	0.03	0.75	0.03	0.84	0.74
Al_2O_3	12.86	0.08	13.73	0.11	13.66	0.42	12.71	0.05	16.04	0.43	15.11	0.37	19.86	1.20	18.24	1.09	13.93	15.64
FeO	8.20	0.12	8.64	0.13	7.06	0.60	8.03	0.07	7.50	0.37	7.30	0.19	6.06	0.42	5.62	0.54	8.63	7.53
MnO	0.20	0.01	0.20	0.02	0.20	0.02	0.17	0.02	0.19	0.01	0.15	0.01	0.22	0.02	0.20	0.01	0.16	0.14
MgO	13.19	0.14	10.84	0.10	9.90	0.28	16.32	0.10	9.49	0.22	8.61	0.16	5.03	0.27	4.37	0.12	10.76	9.51
CaO	7.83	0.07	8.51	0.08	8.48	0.25	6.56	0.05	7.89	0.17	7.77	0.16	8.44	0.43	7.83	0.39	8.50	7.99
Na_2O	2.66	0.05	2.74	0.04	2.72	0.06	2.76	0.03	3.26	0.10	3.57	0.07	3.52	0.16	4.34	0.11	2.76	3.23
K_2O	1.49	0.04	1.64	0.03	1.59	0.08	0.55	0.02	0.66	0.04	0.91	0.03	0.82	0.07	0.99	0.06	1.73	0.93
P_2O_5	0.02	0.02	0.36	0.03	0.46	0.03	0.21	0.02	0.21	0.03	0.22	0.02	0.31	0.02	0.33	0.03	0.37	0.17
X_{H_2O}[b]					0.73						0.73				0.70			
H_2O (wt.%)					2.74						2.77				2.74			
H_2O / CO_2(molar)					2.73						2.77				2.30			

[a] from Ponomareva et al. [2007]

[b] molar H_2O / (H_2O + CO_2)

Table 2: Experimental run conditions. Phase proportions (in parentheses) were determined using the MATLAB program LIME [Prissel et al. 2023], and uncertainties can be found in Table 3, and Goltz [2026] Tables S1, S2, and S3. Fe loss was determined using the method presented in Prissel et al. [2023], and Na loss to fluid was determined by comparing the composition calculated using the LIME best estimate with the bulk composition

ID	Mix	T (°C)	P (GPa)	t (hrs)	Volatiles added (bulk)	Equilibrium assemblage	Capsule material	Fe loss to capsule (%)	Na loss to fluid (%)
hiK tephra-related starting compositions									
OD102[a]	53	1050	1	47.30	H_2O Sat.	g(59)+ol[b](18)+cpx(19)+amph(4)	Au	−5.03	−39.1
F136[a]	53	1010	1	46.97	H_2O Sat.	g(46)+ol(11)+cpx(12)+amph(30)	Au	2.43	−40.3
OD150	70	1175	1	24.05	Mixed Volatile	g(79)+cpx(10)+opx(11)	$Au_{80}Pd_{20}$	5.11	−22
OD153	70	1140	1	23.90	Mixed Volatile	g(78)+cpx(11)+opx(11)	$Au_{80}Pd_{20}$	−9.03	−17.8
OD155	70	1105	1	26.27	Mixed	g(64)+cpx(21)+opx(15)	$Au_{80}Pd_{20}$	5.5	−20
F204	60	1075	1	27.07	H_2O Undersat.	g(70)+ol(9)+cpx(19)+opx(2)	Au	−14.9	−54.6
OD143[a]	60	1060	1	46.90	H_2O Undersat.	g(46)+cpx(22)+opx(6)+amph(26)	Au	−17.7	−51.3
F153	60	1050	1	48.53	H_2O Sat.	g(73)+ol(11)+cpx(16)	Au	−13.4	−29.8
OD173	60	1025	1	24.03	H_2O Sat.	g(70)+ol(10)+cpx(20)	Au	−11.9	−49.8
F163[a]	60	1000	1	47.73	H_2O Sat.	g(49)+ol(3)+cpx(9)+opx(3)+amph(36)	Au	−10.7	−43.4
F149	60	950	1	49.47	H_2O Sat.	g(44)+opx(8)+amph(45)+ap(3)	Au	−7.26	−57.3
F230	70	1080	0.5	12.20	Mixed Volatile	g(75)+ol(5)+cpx(13)+opx(7)	Au	−11.7	−13.6
F175	60	1000	0.5	48.60	H_2O Sat.	g(68)+ol(12)+cpx(20)	Au	−14.1	−45.9
F174[a]	60	950	0.5	47.57	H_2O Sat.	g(39)+opx(3)+amph(57)+ap(1)	Au	−6.15	−40.8
loK tephra-related starting compositions									
F125	54	1100	1	24.17	H_2O Sat.	g(76)+ol(24)	Au	−7.67	−36
F145	54	1050	1	23.83	H_2O Sat.	g(61)+ol(26)+cpx(13)	Au	−10.6	−47.5
F137[a]	54	1010	1	47.30	H_2O Sat.	g(42)+ol(22)+amph(36)	Au	−7.41	−35.5
OD172	73	1125	1	21.20	Mixed Volatile	g(76)+cpx(9)+opx(16)	$Au_{80}Pd_{20}$	−9.09	−26.3
OD170	73	1100	1	19.90	Mixed Volatile	g(75)+cpx(10)+opx(15)	$Au_{80}Pd_{20}$	−0.3	−22.6
OD142	59	1100	1	47.87	H_2O Undersat.	g(75)+cpx(14)+opx(11)	Au	−15.1	−56.4
OD163	59	1100	1	24.03	H_2O Sat.	g(91)+ol(9)	Au	−5.35	−1.24
OD171	73	1075	1	19.07	Mixed Volatile	g(69)+cpx(13)+opx(16)+plag(2)	Au	−10.9	−16.2
OD167	59	1075	1	23.03	H_2O Sat.	g(90)+ol(10)	Au	−3.59	−18.6
OD144[a]	59	1060	1	47.03	H_2O Undersat.	g(40)+cpx(1)+opx(2)+amph(57)	Au	−9.66	−41.5
OD169	73	1050	1	18.92	Mixed Volatile	g(46)+cpx(12)+opx(11)+amph(22)+plag(9)	Au	1.02	−20.1
OD161	59	1050	1	43.20	H_2O Sat.	g(83)+ol(10)+cpx(8)	Au	−13.7	−56.2
OD160	59	1025	1	29.03	H_2O Sat.	g(77)+ol(9)+cpx(14)	Au	−11.9	−48.7
OD166	59	1010	1	21.87	H_2O Sat.	g(77)+ol(9)+cpx(14)	Au	−4.48	−45.5
OD109[a]	59	1000	1	51.97	H_2O Sat.	g(59)+opx(3)+amph(38)	Au	−1.96	−39.5
OD168	59	975	1	22.97	H_2O Sat.	g(51)+opx(2)+amph(47)	Au	4.4	−35.2
F231	73	1205	0.5	13.03	Mixed Volatile	g(92)+opx(8)	$Au_{80}Pd_{20}$	17.3	−8.08
F236	73	1155	0.5	13.00	Mixed Volatile	g(55)+cpx(10)+opx(17)+plag(18)	$Au_{80}Pd_{20}$	4.17	−9.75
F228	59	1080	0.5	12.30	H_2O Sat.	g(91)+ol(9)	Au	−7.81	−38.7
F233	59	1055	0.5	12.27	H_2O Sat.	g(89)+ol(11)	Au	−0.19	−29.5
F237	76	1030	0.5	12.27	H_2O Sat.	g(96)+ol(1)+cpx(3)	Au	−7.34	−25.1
F243	76	980	0.5	21.97	H_2O Sat.	g(81)+amph(19)	Au	−9.75	−36.4
F246	76	955	0.5	21.30	H_2O Sat.	g(79)+amph(21)	Au	−9.19	−34.3
OD178	79	1075	1	22.80	Mixed Volatile	g(94)+cpx(4)+opx(2)	Au	−10.3	−15.2
OD177	79	1025	1	24.27	Mixed Volatile	g(33)+cpx(8)+opx(9)+amph(4)+plag(46)	Au	−17.4	−13.6
OD174	76	1000	1	24.23	H_2O Sat.	g(87)+cpx(2)+amph(11)	Au	−9.52	−34.5
OD175	76	950	1	22.20	H_2O Sat.	g(75)+amph(25)	Au	−0.71	−37.4
OD179	76	925	1	21.32	H_2O Sat.	g(66)+amph(34)	Au	−4.73	−40.3
OD176	76	900	1	24.13	H_2O Sat.	g(65)+amph(32)+plag(3)	Au	−13.2	−42.4
F241	79	1055	0.5	19.60	Mixed Volatile	g(100)	Au	−20.1	−12.1
F242	79	1005	0.5	22.17	Mixed Volatile	g(62)+cpx(16)+opx(4)+plag(18)	Au	−8.95	−24.5
F245	79	980	0.5	21.60	Mixed Volatile	g(55)+cpx(19)+opx(5)+plag(21)	Au	−20.78	−28.1

[a] Indicates an experiment previously published in Goltz et al. [2022]

[b] Sum of proportions of olivine cores and rims; see Table 3 and Section 3 for discussion

Note: g = glass; ol = olivine; opx = orthopyroxene; cpx = clinopyroxene; plag = plagioclase; amph = amphibole; ap = apatite

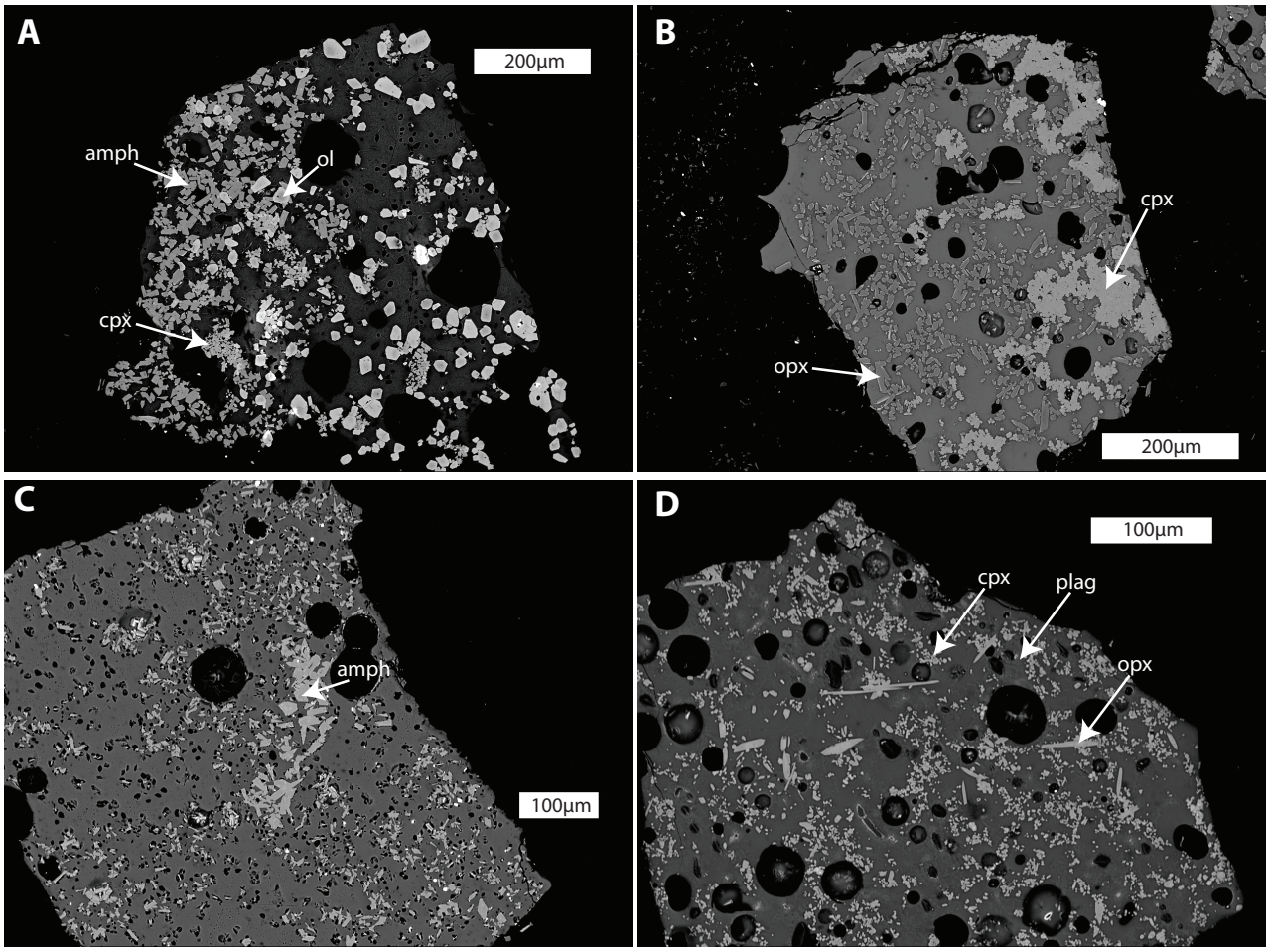

Figure 1: Back-scattered electron images of experiments [A] F136, [B] OD153, [C] F243, and [D] F242. Note frothy and vesiculated glass in water saturated experiments ([A] and [C]) as compared to glass in mixed volatile experiments ([B] and [D]). Phase abbreviations used throughout this text and tables (see also Table 2): ol = olivine, opx = orthopyroxene, cpx = clinopyroxene, plag = plagioclase, amph = amphibole, ap = apatite, g = glass.

results calculated using LIME [Prissel et al. 2023] show that some proportion of Na_2O added to our capsules was lost during our experiments, likely to a fluid phase. The loss across all experiments varied from 1.2 % to 57 %. On average, for saturated experiments, loss was 39 ± 11 %; for mixed-volatile experiments, the average loss was 18 ± 6 % (Table 2). The stability of phases in our experiments are self-consistent despite different degrees of alkali and iron loss (Section 3.1), so the impact of alkali and iron loss on phase stability is minimal, though compositions of phases (especially melt/glass) in the experiments are likely depleted in alkalis.

To prevent excessive iron loss, gold capsules were used in experiments run at or below 1100 °C. For higher temperature experiments, Fe-saturated gold-palladium (80:20) capsules were used. The capsules were saturated using a method after Blatter et al. [2013]. To saturate the $Au_{80}Pd_{20}$ capsules, the capsules were packed with and surrounded by a 2:1 mixture by weight of magnetite and clear jewelry enamel in a large Pt crucible. The packed crucible was suspended in a gas mixing furnace at 1100 °C with a flow of CO_2-H_2 gas to control the f_{O_2} at NNO for about a week, after which the crucible and capsules were cleaned by immersion and sonication in hydrofluoric acid for 2–4 days. Success of the Fe-saturation procedure was confirmed by measurement of Fe in two saturated capsules using EPMA. We analyzed 34 line-scans using a traditional background correction method (rather than the mean atomic number correction used for our analyses of silicates) across the two capsules and found that the alloy was $Au_{78}Pd_{19}Fe_3$ throughout, approximately consistent with values calculated using the equations and procedure of Balta et al. [2011]. For these analyses, we used the nominally iron-free $Au_{80}Pd_{20}$ tubing used to form the capsules before iron saturation as a primary standard for gold and palladium and a National Bureau of Standards (NIST) stainless steel standard (NBS160a) as the primary standard for iron. Success of the Fe-saturation of $Au_{80}Pd_{20}$ capsules was also evaluated using a mass balance calculation of Fe-loss for all experiments (see method in Prissel et al. [2023]). The maximum Fe-loss

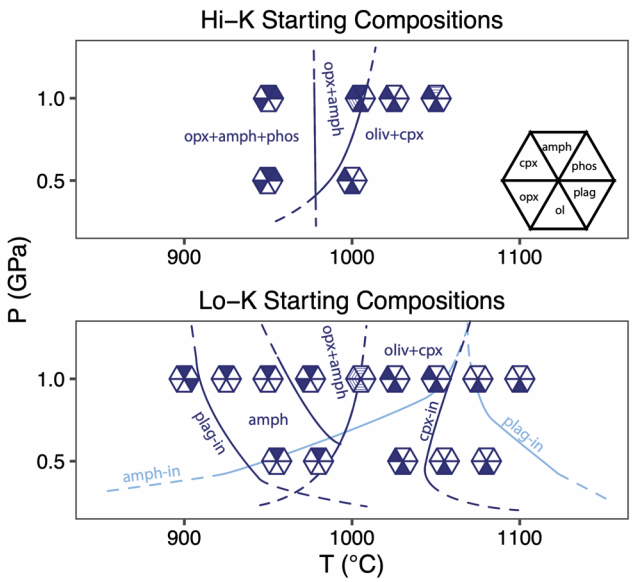

Figure 2: Diagrams summarizing the stability of phases in our experiments on hi-K and lo-K related starting compositions. Hexagons and dark blue lines show the stability of phases in H_2O-saturated experiments; phase boundaries in light blue show the stability of phases in mixed volatile experiments (hexagons not pictured). Filled wedges correspond to stability of phases, as represented in the legend in the upper diagram. At 1000 °C and 1 GPa in the lo-K starting composition, we represent the results of experiments F137, OD166, and OD109 with a single hexagon. These experiments differ in the starting mix used and in temperature (a difference of 10 °C), and contain some combination of olivine, orthopyroxene, clinopyroxene, and amphibole, which we notate with the partially filled hexagons. The discrepancies between these three experiments indicate our proximity to a point in *P-T* space where all four phases co-exist before the olivine and pyroxenes are fully consumed to produce amphibole via peritectic reaction. At 1000 °C and 1 GPa in the hi-K starting compositions, we summarize the results of experiments F136 and F163, which differ in starting mix and in temperature by 10 °C, where one contains orthopyroxene and the other does not. This *P-T* condition also represents a point prior to the consumption of pyroxenes and olivine to produce amphibole via peritectic reaction. At 1050 °C and 1 GPa in the hi-K starting compositions, we summarize experiments OD102 and F153 with a single hexagon. These experiments differ in starting mix, and only one contains minor (i.e. 4 %) amphibole, which we indicate with the partially filled amphibole hexagon wedge.

observed in successful experiments was ~21 %, but the average Fe-loss in the AuPd capsules was much more moderate in general, averaging 6 % (Table 2). Some experiments show evidence for up to 17 % Fe gain (Table 2). As experiments with varying degrees of Fe loss are self-consistent and Mg-Fe systematics vary consistently with decreasing temperature, we believe that neither Fe loss nor Fe gain substantially impacts our results and do not discuss this aspect further.

2.2 Experimental procedures

2.2.1 *Capsule design*

Experiments used a nested capsule design following Matjuschkin et al. [2015]. although our design uses crushable MgO above and below the capsule. A Pt buffer capsule packed with 20–30 mg of a 5:1 molar mixture of Ni:NiO and an Au or $Au_{80}Pd_{20}$ sample capsule packed with 30 mg of the starting mix were surrounded with and separated by Al_2O_3 powder in a larger diameter gold or gold palladium outer capsule. For water saturated and water undersaturated experiments with no mixed volatiles, free water was added to all capsules (2 or 3 µL in the Pt buffer capsule, 3 or 6 µL in the sample capsule, and 10 or 20 µL in the outer capsule). For mixed volatile experiments, 1 µL of free water was only added to the Pt buffer capsule and outer capsule to mitigate water loss through diffusion and to equilibrate oxygen fugacity in the experiment with the buffer. After packing, all capsules were crimped straight across (Pt buffer capsule) or in a three-fin design (sample and outer capsules) and welded shut using tungsten-inert gas micro-arc welding. Leaks were checked for by weighing, heating in a 149 °C oven for 2 minutes, and reweighing the capsule three times. After showing no leaks, the outer capsule was compressed to a final height of 7–8.5 mm.

2.2.2 *Piston cylinder*

Experiments were conducted using piston cylinder apparatuses at Washington University in St. Louis at either 1 GPa or 500 MPa using a 12.7 mm or 19.1 mm pressure vessel bore diameter, respectively, and details of the assembly are described in Goltz et al. [2022]. In all experiments, capsules were surrounded by a pyrophyllite sleeve and other pieces within the graphite furnace were made of fired, crushable MgO. Experimental temperature ranged from 900 to 1205 °C and experimental duration ranged from 12 to 52 hours (Table 2).

Experiments at 1 GPa were conducted using a barium carbonate pressure medium. The experiments were first pressurized to 1 GPa and then heated at 50 °C/min to the target temperature, with a 6-minute dwell in the temperature ramp at 865 °C. 500 MPa experiments were run using an assembly with a pyrex or fused silica glass sleeve separating the graphite furnace from the NaCl pressure medium. Pyrex sleeves were used for experiments at temperatures ≤ 1125 °C, and fused silica glass sleeves were used at higher experimental temperatures. For all but two experiments (F174 and F175), samples were pressurized and then heated at 15 °C/min to the target temperature with a 24-minute dwell at 600 °C. F174 and F175 were pressurized and then heated at 50 °C/min to the target temperature with a 6-minute dwell at 600 °C. Details of the experimental calibration of these assemblies, including uncertainty on temperature, are given in the Supplementary Material Text [Goltz 2026].

2.2.3 *Experimental charge evaluation*

In all cases, experimental success was initially evaluated upon inspection of the quenched experimental charge. The outer capsule was punctured with a small drill-bit to confirm the presence of free water in the outer capsule. The outer capsule was then opened and experiments where the sample capsule

had obviously leaked silicate material during the run or where the alumina in the outer capsule was densely recrystallized were considered failures and were not analyzed further. In all successful experiments, we also confirmed the presence of nickel metal and nickel oxide in the platinum capsule visually and by using a magnet. Experiments that appeared successful based on capsule evaluation were subjected to further analysis, and were disqualified from inclusion if crystals were strongly zoned in major elements consistent with the effects of Fe-loss, had a mineral-melt FeO_{tot}-MgO $K_D > 0.40$ for olivine, displayed open system behavior in the form of Fe-loss, or had a proportion of glass calculated by mass balance inconsistent with that of bracketing higher and lower temperature experiments. In this manuscript, we only report successful experiments.

2.3 Analytical methods

The major element compositions of synthetic products were determined by electron probe microanalysis (EPMA). Analyses were performed on a JEOL JXA-8200 electron microprobe using five wavelength-dispersive spectrometers. The background correction method (using a mean atomic number background; Donovan and Tingle [1996]), analytical conditions, and analytical standards are identical to those described in Goltz et al. [2022]. A time dependent intensity correction was applied to glass analyses in experiment F174; the details of that correction are described in Goltz et al. [2022].

3 Results

3.1 Approach to equilibrium

While the long durations of our experiments and limited iron loss from our experimental charges encourage equilibrium, they are insufficient to demonstrate that equilibrium was achieved. Several aspects of our experimental charges are consistent with the achievement of equilibrium. First, phases in our experiments are relatively homogeneous. To analyse our experiments, we first crushed the experimental products to produce chips typically hundreds of microns in size. We then mounted three or more randomly selected chips in ~1/4" diameter brass rings. The chips were then imaged and analysed using EPMA, as described in Section 2.3. Thus, our analyses are of phases from throughout the experimental charge. The phases are relatively homogenous, as exemplified by the relatively small standard deviation of phase compositions as determined from EPMA analysis (see also the lack of zoning in phases in Figure 1). Only one of our experiments, OD102, proves an exception to this: olivine in this experiment is normally zoned from core to rim (i.e. rims are lower in Mg#; Table 3, Supplementary Material [Goltz 2026] Figure S1). Such normal zonation cannot be an effect of Fe-loss to the capsule, which would produce reverse zonation in the olivine. Because the cores constitute a relatively minor volumetric percentage of the charge as calculated by mass balance, the range in Mg# is restricted from core to rim (84 to 79; Table 3), and $K_D^{Fe\text{-}Mg}$ is not abnormal, we do not exclude this experiment from our analysis. Secondly, there are consistent changes in phase assemblages and proportions with decreasing temperature. As evidenced in phase diagrams (Figure 2), phase boundaries are regular. Table 3 demonstrates that, as temperature decreases, for a given starting mixture, crystallinity increases (i.e. percent glass in the charge decreases). Between starting mixes, there is some minor variability in phase appearances. For example, an experiment conducted using mix #53 as a starting composition is saturated with amphibole at 1050 °C (OD102; Table 2), while another experiment run at the same temperature but using mix #60 (related to mix #53 through the fractionation of olivine, see Section 2.1) is not saturated with amphibole (F153; Table 2). However, for a given starting composition at a given water content, phase stability is self-consistent, suggesting attainment of equilibrium. Together, these factors suggest that equilibrium was attained in the experiments reported here.

3.2 General observations

Observed phases in our experiments include olivine, clinopyroxene, orthopyroxene, amphibole, plagioclase, liquid (i.e. glass), and minor apatite (Table 2). As in Marxer et al. [2023], the lack of early crystallizing oxide minerals could be related to the lack of Cr in our experimental starting mixes and a slightly lower oxygen fugacity of our experiments compared to others where oxide phases saturate at higher temperatures. Crystal size varies from ~1 μm to ~200 μm, with clinopyroxene and minor phases usually among the smallest analyzed phases and amphibole and plagioclase among the largest. Crystals appear unzoned in major elements (Figure 1), except in experiment OD102 where crystals are zoned from core to rim in Mg and Fe (Table 3). Glass in all experiments is vesicular, and glass in H_2O-saturated experiments at 1 GPa is also devitrified due to their high H_2O contents and difficulty quenching high pressure hydrous melts to glass [Gavrilenko et al. 2019].

3.3 Phase relations

In this study, we conducted experiments at pressures of 500 MPa and 1 GPa and at temperatures ranging from 900–1205 °C (Table 2, Figure 2). At 1 GPa, for mixes related to the hi-K tephra, we conducted experiments from 950–1175 °C; at 500 MPa, experiments ranged in temperature from 950–1080 °C. At 1 GPa, for mixes related to the lo-K tephra, we conducted experiments from 900–1125 °C; at 500 MPa, experiments ranged in temperature from 955–1205 °C. H_2O-saturated experiments have olivine as the liquidus phase, whereas the highest temperature runs in H_2O-undersaturated experiments contained ortho- and clino-pyroxene, consistent with a higher activity of SiO_2 in the melt favoring orthopyroxene over olivine crystallization [e.g. Sisson and Grove 1993; Koch et al. 2025]. Relatively higher temperature stability of plagioclase in H_2O-undersaturated experiments compared to H_2O-saturated runs is observed and was expected due to the suppression of plagioclase at high water contents [e.g. Yoder and Tilley 1962; Holloway and Burnham 1972; Sisson and Grove 1993]. Phase relations in all our experiments are tabulated in Table 2 and we present a phase diagram with our results in Figure 2.

3.3.1 *H_2O-saturated experiments (mixes 53, 54, 59, 60, 54, 59, and 76)*

Olivine is the highest temperature crystallizing phase in H_2O-saturated experiments on the lo-K tephra starting compositions (mixes 54, 59, and 76). In 1 GPa experiments on the lo-K tephra starting mix, clinopyroxene joins the equilibrium assemblage between 1075 and 1050 °C. Between 1010 and 975 °C at 1 GPa, amphibole and orthopyroxene crystallize and olivine and clinopyroxene are no longer part of the crystallizing assemblage. Plagioclase crystallizes at temperatures below 925 °C at 1 GPa.

We did not determine the liquidus phase in H_2O-saturated experiments on the hi-K tephra starting compositions, but our highest temperature runs at 1050 °C had equilibrium assemblages of olivine + clinopyroxene (mix 60) or olivine + clinopyroxene + amphibole (mix 53). In both starting mixes at 1 GPa, amphibole is present below 1025 °C. At 500 MPa, amphibole is in equilibrium with melts below 1000 °C.

A key aspect of our results is the identification of a pressure-temperature condition—~1000 °C and 1 GPa at water saturated conditions—that captures a peritectic reaction in progress to produce amphibole in both starting compositions. At this pressure-temperature condition, olivine, clinopyroxene, orthopyroxene, and amphibole co-exist before the full consumption of the olivine and pyroxene phases to produce amphibole in a peritectic reaction at lower temperatures [e.g. Blatter et al. 2017; 2023] (Figure 2).

The temperatures at which amphibole stabilizes in our water saturated experiments are likely minima. Excess fluids and subsequent alkali loss, which we observe in our experiments (see Section 2) can impact the stability of amphibole. Mandler and Grove [2016] and Putak Juriček and Keppler [2023] show that the amphibole stability field in peridotite decreases in size with increasing water content as a result of alkali loss. In our experiments, it is more challenging to disentangle the impacts of alkali loss and increasing H_2O contents. Mixed volatile and H_2O-undersaturated experiments stabilize amphibole at higher temperatures than H_2O-saturated experiments at the same pressure (Figure 2, Table 2). However, at lower water contents, amphibole stability occurs at higher crystallinity. Among lo-K starting compositions, amphibole comes in at 1000 °C and 41 % crystallization for H_2O-saturated experiments, 1060 °C and 60 % crystallization for H_2O-undersaturated conditions, and 1050 °C and 54 % crystallization for mixed-volatile experiments (Table 2). So, while amphibole comes in at lower T in H_2O-saturated experiments, it also comes in closer to the liquidus, assuming a constant rate of crystallization with respect to decreasing temperature. The lower temperature stability of amphibole for these experiments might thus be linked to the depressed liquidus in the H_2O saturated system, rather than to alkali loss. It is possible that, in the absence of alkali loss, amphibole may stabilize even closer to the liquidus, so our experiments can be taken as the minimum T stability of amphibole.

3.3.2 *H_2O-undersaturated, CO_2-free experiments (mixes 59 and 60; 1 GPa only)*

Orthopyroxene + clinopyroxene ± olivine are equilibrium phases in the highest temperature experiments at these conditions. Amphibole is observed in the 1060 °C runs in both starting compositions (i.e. lo-K and hi-K tephra; mixes 59 and 60). Relative to H_2O-saturated experiments, amphibole joins the crystallizing assemblage at higher temperatures (and higher crystallinities; Table 2). Plagioclase was not observed.

3.3.3 *H_2O-undersaturated, mixed-volatile experiments (mixes 70, 73, and 79)*

Orthopyroxene ± clinopyroxene are the equilibrium phases in the highest temperature experiments on mixed volatile experiments. In experiments on the lo-K tephra starting composition (mixes 73 and 79), plagioclase joins the crystallizing assemblage between 1100 and 1025 °C at 1 GPa or between 1205 and 1055 °C at 500 MPa. At 1025 °C at 1 GPa, amphibole joins the equilibrium assemblage; amphibole is not observed in experiments with mixed-volatiles at 500 MPa.

3.4 Phase chemistry

The average chemistry of mineral phases and glass in our experiments is summarized in Table 3.

3.4.1 *Olivine*

Olivine composition in our experiments ranges from Fo_{76} to Fo_{88} (Table 3). The Fe-Mg mineral-melt exchange coefficient (Fe-Mg K_D, calculated assuming all Fe is FeO) of olivine ranges from 0.25–0.35 (Figure 3, Table 3). The median Fe-Mg K_D is 0.29, consistent with other experimentally determined values [e.g. Roeder and Emslie 1970]. Olivine coexisting with amphibole ranged from Fo_{77} to Fo_{84}.

3.4.2 *Amphibole*

Amphibole composition in our experiments ranges from Mg# 66 to 84 (where Mg# is calculated Mg / (Mg + Fe_{tot}) all in moles), in Al_2O_3 from 11 to 16 wt.%, and in TiO_2 from 1.1–3.7 wt.% (Figure 4, Table 3). Amphibole in the mixed volatile experiments have high concentrations of TiO_2 relative to the water saturated experiments. The higher titanium content of the amphiboles in equilibrium with lower H_2O content melts is consistent with lower hydroxyl occupancy in its O3 site (i.e. greater oxo component) due to the lower H_2O content of the equilibrium melts and assuming a constant partition coefficient of H between amphibole and melt. Hydrogen content in amphibole is negatively correlated with the sum of Ti, Fe^{3+}, and ^{VI}Al in the amphibole, all of which balance the excess negative charge from the oxo component with excess positive charge in its octahedral sites, assuming no change in halogen content [e.g. King et al. 1999; Oberti et al. 2007]. Given the similar aluminum content of the amphiboles compared to others in this study and the similar experimental f_{O_2} (which should generate a similar Fe^{3+}/Fe^{2+} in the amphibole; e.g. King et al. [2000] and Goltz et al. [2022]), the potentially lower hydroxyl content of amphiboles in the lower H_2O content experiments would require more titanium for charge balance.

Table 3: Compositions and proportions of synthetic phases in oxide wt.%. *n* is number of analyses. Glass compositions are reported normalized to 100 with the un-normalized total. Numbers in italics are the 1 standard deviation of repeated analyses. Iron is reported as total iron as ferrous (FeO_{tot}). Mg# is calculated as $Mg/(Mg+Fe_{tot})$. Phase proportions are given as the best fitting phase abundance and the difference between the fit and the 25th and 75th percentiles of the probability density function output by LIME (−25% and +75%, respectively). Reporting error in this way reflects the asymmetry of the LIME algorithm's output; see [Prissel et al. 2023] for more details on the best practices on reporting phase proportions. 1 standard deviation of repeated analyses reported in Supplementary Material [Goltz 2026] Table S3.

Run	Phase	*n*	Proportion (-25%/+75%)	SiO_2	TiO_2	Al_2O_3	FeO_{tot}	MnO	MgO	CaO	Na_2O	K_2O	P_2O_5	Total	Mg #	$K_D^{Fe\text{-}Mg}$	D_{Ti}
OD102	g	20	58.8 (-3.0/+0.4)	56.73	1.03	20.25	5.96	0.16	3.88	7.55	2.41	2.02	BDL	88.47	0.54		
	ol (rims)	11	13.0 (-2.2/+1.9)	38.74	0.03	BDL	19.35	0.38	40.93	0.13	BDL	BDL	BDL	99.57	0.79	0.31	
	ol (cores)	12	4.8 (-1.7/+2.4)	39.85	0.06	0.04	15.11	0.36	44.58	0.2	BDL	BDL	0.02	100.24	0.84	0.22	
	cpx	13	19.3 (-1.5/+0.6)	52.89	0.41	2.32	5.61	0.2	16.67	22.03	0.27	0.02	BDL	100.42	0.84	0.22	
	amph	10	4.1 (-1.8/+2.9)	43.33	1.93	12.96	7.89	0.16	16.6	11.42	2.36	0.83	0.02	97.5	0.79	0.31	1.9
F136	g	17	46.0 (-3.5/+0.9)	60.67	0.66	19.04	6	0.17	3.06	6.35	1.9	2.13	0.03	88.9	0.48		
	ol	17	11.4 (-1.5/+1.0)	39.1	0.03	0.02	20.44	0.41	39.98	0.15	BDL	BDL	BDL	100.15	0.78	0.26	
	cpx	19	12.1 (-3.8/+4.9)	53.03	0.43	2.44	6.89	0.27	16.14	20.88	0.36	0.03	0.02	100.48	0.81	0.22	
	amph	22	30.4 (-7.2/+6.6)	44.62	1.52	11.63	8.3	0.15	16.44	11.43	2.14	0.93	BDL	97.15	0.78	0.26	2.3
OD150	g	14	79.2 (-1.5/+1.0)	54.39	1.01	16.6	7.47	0.17	6.39	8.89	2.64	1.84	0.6	92.13	0.6		
	cpx	7	10.0 (-1.4/+1.7)	52.58	0.26	2.24	5.72	0.2	18.44	19.64	0.28	BDL	BDL	99.39	0.85	0.27	
	opx	12	10.8 (-1.0/+1.1)	55.9	0.14	1.52	8.5	0.26	31.17	2.3	0.04	BDL	BDL	99.86	0.87	0.23	
OD153	g	14	77.7 (-1.5/+1.1)	55.17	1.05	17.28	6.26	0.17	6.25	8.49	2.83	1.88	0.63	90.64	0.64		
	cpx	14	11.3 (-1.5/+1.7)	53.72	0.32	2.29	5.1	0.22	18.44	19.82	0.3	0.02	BDL	100.23	0.87	0.28	
	opx	13	11.0 (-1.0/+1.1)	55.59	0.19	1.84	9.18	0.28	30.87	2.02	0.03	BDL	BDL	100	0.86	0.30	
OD155	g	17	63.7 (-1.4/+1.2)	54.89	1.14	19.63	6.99	0.16	3.83	6.96	3.25	2.38	0.77	91.25	0.49		
	cpx	13	20.9 (-1.5/+1.5)	52.15	0.52	3.91	6.25	0.25	16.84	19.43	0.47	0.05	0.03	99.88	0.83	0.20	
	opx	12	15.4 (-1.1/+1.2)	53.83	0.26	3.43	10.92	0.3	28.54	1.99	0.05	0.02	BDL	99.36	0.82	0.21	
F204	g	16	69.5 (-1.6/+0.3)	56.14	1.04	19.45	7.07	0.16	4.44	7.7	1.61	1.87	0.52	88.78	0.53		
	ol	7	9.3 (-1.0/+1.0)	37.51	0.03	0.05	18.41	0.31	42.55	0.17	BDL	BDL	0.13	99.17	0.8	0.27	
	cpx	9	19.4 (-1.4/+1.2)	52.28	0.61	1.66	5.54	0.19	16.98	21.58	0.62	0.02	0.02	99.51	0.85	0.20	
	opx	10	1.8 (-0.8/+1.6)	53.4	0.18	2.17	11.69	0.33	29.56	1.58	0.02	BDL	BDL	98.93	0.82	0.25	
OD143	g	9	45.9 (-2.0/+1.8)	57.08	0.91	20.21	6.73	0.16	3.88	7.62	1.31	1.46	0.64	88.49	0.51		
	cpx	7	21.8 (-1.4/+1.2)	52.73	0.5	3.14	6.81	0.26	16.37	20.26	0.54	0.03	0.11	100.75	0.81	0.24	
	opx	9	6.3 (-1.0/+1.1)	53.64	0.22	3.64	13.48	0.34	27.57	1.65	0.03	BDL	BDL	100.59	0.78	0.28	
	amph	10	26.0 (-1.9/+1.8)	42.79	1.96	13.93	8.45	0.14	16.14	11.07	2.31	1.03	0.04	97.86	0.77	0.30	2.2
F153	g	13	72.7 (-0.9/+0.9)	53.98	0.96	19.27	6.78	0.17	4.99	8.95	2.61	1.83	0.47	88.66	0.57		
	ol	13	11.0 (-0.6/+0.6)	39.35	0.04	0.02	18.13	0.36	42.26	0.2	BDL	BDL	0.24	100.58	0.81	0.32	
	cpx	8	16.3 (-0.8/+0.9)	53.15	0.3	1.77	5.33	0.19	16.87	22.52	0.17	BDL	BDL	100.32	0.85	0.23	
OD173	g	19	70.1 (-1.8/+1.6)	56.91	0.99	18.87	6.91	0.16	4.19	7.79	1.79	1.91	0.49	88.44	0.52		
	ol	13	9.8 (-0.7/+0.8)	39.14	0.04	BDL	19.01	0.34	41.3	0.24	BDL	BDL	0.39	100.48	0.79	0.28	
	cpx	17	20.1 (-1.8/+1.9)	53.28	0.65	1.6	5.92	0.19	16.49	21.61	0.59	0.03	0.06	100.44	0.83	0.22	
F163	g	19	49.4 (-3.1/+0.9)	60.44	0.44	19.18	6.29	0.17	3.04	6.64	1.5	1.55	0.75	87.35	0.46		
	ol	13	2.6 (-1.1/+1.7)	38.82	0.02	0.02	21.25	0.4	39.7	0.16	BDL	BDL	0.26	100.65	0.77	0.26	
	cpx	12	9.0 (-1.8/+1.8)	53.27	0.44	2.47	6.79	0.23	15.79	20.58	0.49	0.04	0.05	100.16	0.81	0.21	
	opx	12	2.7 (-1.1/+1.8)	54.06	0.13	2.4	15.78	0.52	26.19	1.44	0.02	BDL	BDL	100.57	0.75	0.29	
	amph	16	36.3 (-4.7/+3.7)	44.9	1.41	11.35	9.49	0.18	16.38	10.94	2.12	0.76	0.03	97.57	0.75	0.28	3.2
F149	g	17	43.6 (-2.1/+1.4)	64.9	0.4	19.49	4.72	0.16	1.34	5.61	0.69	2.1	0.59	86.88	0.33		
	opx	15	8.3 (-1.9/+2.4)	53.62	0.16	2.18	16.52	0.48	25.12	1.55	0.02	0.02	BDL	99.68	0.73	0.19	

Note: g=glass; ol=olivine; opx=orthopyroxene; cpx=clinopyroxene; plag=plagioclase; amph=amphibole; ap=apatite

Table 3 continued.

Run	Phase	n	Proportion (-25%/+75%)	SiO_2	TiO_2	Al_2O_3	FeO_{tot}	MnO	MgO	CaO	Na_2O	K_2O	P_2O_5	Total	Mg #	$K_D^{Fe\text{-}Mg}$	D_{Ti}
F149	amph	18	45 (-4.0/+3.9)	45.71	1.05	11.1	10.51	0.24	15.94	10.63	1.89	0.72	0.05	97.83	0.73	0.19	2.6
	ap	7	3.1 (-0.5/+0.5)	0.47	BDL	0.04	0.74	0.12	0.41	55.85	BDL	0.06	41.04	98.73			
F230	g	19	74.6 (-4.8/+0.8)	57.39	1.03	17.75	5.61	0.15	4.67	7.59	3.09	2.08	0.65	92.78	0.6		
	ol	10	5.2 (-1.9/+2.7)	39.69	0.05	0.03	15.55	0.33	44.32	0.21	BDL	BDL	0.17	100.35	0.84	0.29	
	cpx	16	13.2 (-2.6/+2.2)	53.35	0.52	2.27	5.32	0.27	17.47	20.75	0.3	0.05	0.04	100.35	0.85	0.25	
	opx	9	7.1 (-2.7/+3.9)	55.37	0.29	2.3	9.07	0.33	30.37	2.01	0.03	0.05	0.02	99.83	0.86	0.25	
F175	g	13	68.0 (-0.9/+0.7)	57.56	1.01	19.52	6.11	0.15	3.44	7.82	2.02	1.85	0.52	89.57	0.5		
	ol	15	12.4 (-0.7/+0.8)	39.31	0.03	0.03	20.63	0.39	39.57	0.3	BDL	BDL	0.11	100.37	0.77	0.29	
	cpx	10	19.6 (-0.9/+0.9)	53.41	0.61	2	6.21	0.22	16.01	21.7	0.55	0.03	0.04	100.79	0.82	0.22	
F174	g	16	38.9 (-2.1/+1.5)	65.65	0.32	19.67	4.62	0.17	1.61	5.07	1.47	0.89	0.52	87.92	0.38		
	opx	15	2.8 (-1.1/+1.7)	54.39	0.14	2.05	17.38	0.53	24.7	1.4	0.02	0.03	BDL	100.66	0.72	0.25	
	amph	17	57.1 (-3.2/+2.7)	46.24	1.16	10.82	10.46	0.22	15.76	10.73	1.8	0.63	0.06	97.89	0.73	0.23	3.6
	ap	5	1.2 (-0.3/+0.3)	1.02	0.02	0.18	0.68	0.1	0.46	54.84	0.02	0.08	41.2	98.58			
F125	g	10	75.7 (-0.9/+0.8)	56.72	0.81	17.96	6.14	0.14	6.69	8.08	2.34	0.85	0.26	87.9	0.66		
	ol	16	24.3 (-0.8/+0.9)	40.6	0.02	0.03	11.36	0.2	48.25	0.12	BDL	BDL	0.12	100.7	0.88	0.26	
F145	g	17	61.1 (-2.1/+2.3)	57.43	0.85	19.02	5.56	0.14	4.96	8.47	2.33	1.01	0.25	88.42	0.61		
	ol	22	26.0 (-0.9/+0.7)	40.14	0.03	0.02	13.01	0.26	46.53	0.14	BDL	BDL	0.2	100.34	0.86	0.25	
	cpx	21	13.0 (-1.9/+2.2)	53.26	0.29	2.11	4.85	0.17	17.47	21.79	0.21	BDL	BDL	100.17	0.87	0.25	
F137	g	12	41.8 (-2.0/+2.0)	56.23	0.76	22.27	4.64	0.12	4.59	8.12	2.14	0.85	0.28	88.5	0.64		
	ol	15	21.9 (-0.8/+0.7)	39.82	0.03	0.03	15.53	0.27	44.26	0.13	BDL	BDL	0.3	100.38	0.84	0.35	
	amph	14	36.3 (-2.4/+2.4)	45.21	1.34	12.49	6.2	0.11	17.72	11.43	2.38	0.33	0.02	97.23	0.84	0.35	1.8
OD172	g	15	75.5 (-1.4/+1.2)	57.76	0.9	19.21	5.72	0.13	3.83	7.65	3.4	1.08	0.32	92.74	0.54		
	cpx	11	8.6 (-1.3/+1.4)	51.93	0.51	4.96	6.95	0.25	16.35	18.4	0.55	0.03	0.03	99.97	0.81	0.28	
	opx	10	15.9 (-0.8/+0.8)	53.83	0.25	4.03	11.57	0.28	28.03	2.13	0.07	BDL	BDL	100.22	0.81	0.28	
OD170	g	15	75.0 (-1.1/+0.8)	57.92	0.88	20.07	5.92	0.12	3.04	6.91	3.59	1.19	0.36	92.05	0.48		
	cpx	14	10.2 (-1.1/+1.3)	51.94	0.54	4.33	8.43	0.25	15.95	18.24	0.58	0.02	0.02	100.31	0.77	0.27	
	opx	13	14.8 (-0.8/+0.8)	53.13	0.27	4.3	13.85	0.3	26	2.02	0.06	BDL	BDL	99.97	0.77	0.27	
OD142	g	15	74.6 (-1.1/+0.9)	56.65	0.89	20.42	6.06	0.16	4.7	8.32	1.84	0.67	0.29	88.86	0.58		
	cpx	14	14.4 (-1.2/+1.2)	53.35	0.33	2.77	5.65	0.22	17.47	20.29	0.33	BDL	BDL	100.42	0.85	0.25	
	opx	21	11.1 (-0.8/+0.8)	54.93	0.18	3.16	9.89	0.31	29.94	1.73	0.03	BDL	BDL	100.17	0.84	0.26	
OD163	g	14	91.4 (-0.7/+0.6)	55.62	0.81	17.66	6.43	0.17	6.01	8.74	3.53	0.81	0.23	87.82	0.62		
	ol	4	8.6 (-0.6/+0.7)	37.4	0.02	0.03	14.56	0.3	46.74	0.13	BDL	BDL	0.03	99.21	0.85	0.29	
OD171	g	16	69.2 (-2.2/+1.3)	58.34	0.96	20.09	5.27	0.12	2.95	6.44	4.05	1.4	0.38	92.98	0.5		
	cpx	9	12.6 (-1.0/+0.8)	52.14	0.71	5.35	7.29	0.23	15.38	18.8	0.6	0.04	0.03	100.57	0.79	0.27	
	opx	10	15.9 (-1.0/+1.3)	53.5	0.31	4.69	13.41	0.28	25.86	1.86	0.07	0.03	0.02	100.03	0.77	0.29	
	plag	11	2.2 (-1.0/+1.9)	52.83	0.05	29.61	0.38	BDL	0.2	12.28	4.53	0.15	BDL	100.04			
OD167	g	17	90.3 (-0.7/+0.7)	55.97	0.82	18.65	6.33	0.17	5.57	8.66	2.94	0.66	0.23	89.09	0.61		
	ol	6	9.7 (-0.7/+0.7)	38.85	0.06	0.02	16.01	0.32	44.69	0.19	BDL	BDL	0.3	100.44	0.83	0.32	
OD144	g	13	40.3 (-3.4/+2.2)	58.56	0.77	20.67	5.74	0.17	3.44	8.53	1.03	0.77	0.32	86.66	0.51		
	cpx	7	1.1 (-0.6/+1.2)	52.48	0.49	3.51	6.41	0.22	16.28	20.86	0.47	BDL	0.02	100.74	0.82	0.24	
	opx	9	1.7 (-0.8/+1.4)	53.16	0.22	4.79	11.97	0.32	28.4	1.69	0.05	BDL	BDL	100.61	0.81	0.25	
	amph	9	56.9 (-4.3/+2.5)	44.01	1.59	13.62	8.25	0.16	16.95	10.76	2.57	0.32	0.02	98.25	0.79	0.29	2.1
OD169	g	19	45.9 (-4.2/+1.8)	61.25	1.12	19.6	4.77	0.1	1.8	4.98	3.7	2.11	0.56	88.25	0.4		
	cpx	13	12.3 (-2.3/+2.1)	51.91	0.86	5.67	8.12	0.23	14.75	17.95	0.66	0.06	0.04	100.25	0.76	0.21	

Note: g=glass; ol=olivine; opx=orthopyroxene; cpx=clinopyroxene; plag=plagioclase; amph=amphibole; ap=apatite

Table 3 continued.

Run	Phase	n	Proportion (-25%/+75%)	SiO_2	TiO_2	Al_2O_3	FeO_{tot}	MnO	MgO	CaO	Na_2O	K_2O	P_2O_5	Total	Mg #	$K_D^{Fe\text{-}Mg}$	D_{Ti}
OD169	opx	15	10.9 (-2.4/+2.4)	52.62	0.35	4.46	14.78	0.31	25.06	2.08	0.11	0.03	0.02	99.81	0.75	0.22	
	amph	15	21.9 (-4.9/+5.0)	42.25	3.7	12.86	11.33	0.18	14.15	9.82	2.63	0.46	0.06	97.45	0.69	0.30	3.3
	plag	11	9.1 (-2.6/+2.9)	53.83	0.07	29.57	0.42	BDL	0.1	11.18	5.03	0.21	BDL	100.41			
OD161	g	15	82.7 (-1.2/+0.9)	57.24	0.75	19.23	5.63	0.18	4.92	8.41	2.66	0.74	0.26	87.88	0.61		
	ol	14	9.6 (-0.7/+0.7)	39.61	BDL	BDL	17.02	0.35	42.62	0.13	BDL	BDL	0.07	99.81	0.82	0.35	
	cpx	14	7.8 (-1.1/+1.3)	53.9	0.31	1.96	4.98	0.21	17.08	21.49	0.29	BDL	0.02	100.25	0.86	0.25	
OD160	g	15	76.7 (-1.2/+1.1)	58.06	0.78	20.05	5.77	0.16	4.08	7.75	2.1	1	0.26	88.59	0.56		
	ol	11	8.9 (-0.6/+0.6)	39.65	0.04	0.07	16.53	0.34	42.68	0.44	BDL	BDL	0.24	100	0.82	0.27	
	cpx	11	14.4 (-1.3/+1.4)	53.6	0.33	2.44	6.04	0.22	16.52	20.88	0.46	BDL	BDL	100.53	0.83	0.26	
OD166	g	16	77.3 (-1.2/+1.0)	57.17	0.87	19.74	6.14	0.16	4.33	7.94	2.12	1.26	0.27	88.75	0.56		
	ol	7	8.9 (-0.7/+0.7)	39.2	0.02	BDL	19.36	0.37	41.48	0.12	BDL	BDL	0.08	100.62	0.79	0.33	
	cpx	7	13.9 (-1.2/+1.3)	53.26	0.59	2.06	6.37	0.2	16.46	20.68	0.99	BDL	0.05	100.67	0.82	0.27	
OD109	g	15	59.2 (-2.1/+1.3)	59.58	0.56	19.71	6.2	0.19	3.55	7.13	1.85	0.89	0.34	87.78	0.51		
	opx	11	3.0 (-1.0/+1.5)	54.77	0.15	2.47	12.71	0.4	28.56	1.36	0.02	BDL	BDL	100.44	0.8	0.25	
	amph	34	37.8 (-2.6/+2.4)	45.48	1.12	11.63	8.57	0.18	17.09	10.94	2.27	0.29	0.02	97.58	0.78	0.29	2.0
OD168	g	10	51.1 (-2.3/+1.5)	61.81	0.51	20.1	5.44	0.16	2.55	6.04	2.11	0.9	0.39	87.8	0.45		
	opx	8	2.2 (-0.9/+1.5)	54.08	0.15	2.39	15.04	0.45	26.72	1.25	BDL	BDL	BDL	100.1	0.76	0.26	
	amph	8	46.6 (-2.7/+2.3)	45.64	1.06	12.21	9.92	0.21	16.22	10.49	2.17	0.27	0.05	98.23	0.74	0.29	2.1
F231	g	20	92.4 (-0.7/+0.6)	54.51	0.78	16.23	8.52	0.16	6.68	8.38	3.54	0.94	0.25	97.04	0.58		
	opx	12	7.6 (-0.6/+0.7)	55.52	0.14	2	9.04	0.24	31.55	1.88	0.03	BDL	BDL	100.42	0.86	0.22	
F236	g	19	55.4 (-2.4/+2.1)	56.55	1.02	16.71	8.39	0.16	4.1	7.06	4.23	1.47	0.32	96.5	0.47		
	cpx	9	9.6 (-1.2/+1.3)	50.31	0.48	4.61	8.47	0.24	16.11	18.63	0.52	0.02	BDL	99.38	0.77	0.26	
	opx	9	17.0 (-1.0/+0.9)	54.89	0.22	2.49	10.52	0.27	29	2.47	0.05	BDL	BDL	99.92	0.83	0.18	
	plag	11	18.0 (-1.7/+1.7)	53.2	0.07	29.17	1.12	BDL	0.2	11.95	4.56	0.22	BDL	100.51			
F228	g	16	90.6 (-1.2/+1.0)	56.95	0.85	18.74	6.32	0.17	5.29	8.53	2.21	0.72	0.23	90.15	0.6		
	ol	5	9.4 (-1.0/+1.2)	39.69	0.02	0.05	16.07	0.35	44.14	0.19	BDL	BDL	0.15	100.67	0.83	0.30	
F233	g	20	88.9 (-0.8/+0.7)	56.79	0.81	18.21	6.42	0.16	4.94	9.17	2.59	0.69	0.22	89.9	0.58		
	ol	14	11.1 (-0.7/+0.8)	39.25	0.03	BDL	16.97	0.35	43.14	0.21	BDL	BDL	0.27	100.25	0.82	0.30	
F237	g	15	95.8 (-2.0/+0.8)	56.76	0.75	19.98	5.45	0.2	4.43	8.47	2.69	1	0.28	88.71	0.59		
	ol	7	1.3 (-0.4/+0.6)	39.71	0.03	0.03	15.99	0.46	43.4	0.35	BDL	BDL	0.14	100.13	0.83	0.30	
	cpx	6	2.9 (-1.1/+1.8)	53.68	0.95	0.84	5.92	0.24	14.84	21.6	2.1	0.02	0.07	100.27	0.82	0.32	
F243	g	15	81.4 (-1.4/+1.3)	59.81	0.56	21.07	4.68	0.21	2.56	7.59	2.19	0.98	0.36	89.05	0.49		
	amph	28	18.6 (-1.3/+1.4)	44.02	1.48	13.4	8.79	0.23	15.51	12.04	2.4	0.4	0.04	98.3	0.76	0.31	2.6
F246	g	15	79.0 (-1.4/+1.4)	60.27	0.51	21.3	4.41	0.2	2.29	7.37	2.28	1.01	0.36	89.02	0.48		
	amph	25	21.0 (-1.4/+1.4)	42.9	1.53	14.44	9.7	0.25	14.59	11.64	2.36	0.41	0.05	97.87	0.73	0.35	3.0
OD178	g	20	94.1 (-1.5/+0.4)	58.61	0.76	20.09	4.85	0.19	3.24	6.78	3.89	1.22	0.36	94.53	0.54		
	cpx	9	3.7 (-1.1/+1.5)	52.42	0.61	4.92	6.86	0.37	15.15	19.78	0.59	0.03	0.03	100.75	0.8	0.30	
	opx	14	2.2 (-0.6/+0.8)	53.19	0.29	5.03	13.88	0.5	25.91	1.84	0.05	BDL	BDL	100.72	0.77	0.36	
OD177	g	15	33.0 (-7.9/+7.4)	62.23	0.86	19.49	4.67	0.18	1.71	5.08	3.69	1.58	0.51	92.24	0.4		
	cpx	10	7.9 (-2.2/+2.2)	52.58	0.62	4.09	7.94	0.42	14.28	19.41	0.74	0.04	0.13	100.25	0.76	0.20	
	opx	16	9.3 (-2.3/+2.0)	52.1	0.32	3.83	19.51	0.59	21.74	1.88	0.07	BDL	0.03	100.07	0.66	0.33	
	amph	14	4.1 (-1.4/+1.7)	42.74	2.97	14.28	11.72	0.28	13.13	10.04	2.69	0.39	0.04	98.28	0.67	0.33	3.5
	plag	9	45.8 (-7.6/+5.7)	54.27	0.1	28.87	0.59	0.04	0.18	10.43	5.14	0.23	0.07	99.91			

Note: g=glass; ol=olivine; opx=orthopyroxene; cpx=clinopyroxene; plag=plagioclase; amph=amphibole; ap=apatite

Table 3 continued.

Run	Phase	n	Proportion (-25%/+75%)	SiO_2	TiO_2	Al_2O_3	FeO_{tot}	MnO	MgO	CaO	Na_2O	K_2O	P_2O_5	Total	Mg #	$K_D^{Fe\text{-}Mg}$	D_{Ti}
OD174	g	18	86.9 (-2.6/+0.7)	59	0.63	20.54	5.2	0.2	2.86	7.7	2.29	1.26	0.32	87.87	0.49		
	cpx	6	2.3 (-1.0/+1.8)	52.88	1.03	1.44	5.43	0.2	14.66	22.33	1.58	0.02	0.11	99.68	0.83	0.20	
	amph	15	10.8 (-1.8/+1.8)	43.6	1.4	13.26	8.02	0.21	16.22	11.59	2.51	0.48	BDL	97.3	0.78	0.27	2.2
OD175	g	19	75.5 (-1.5/+1.4)	60.66	0.53	21.3	4.32	0.19	1.93	7.44	2.09	1.17	0.37	84.97	0.44		
	amph	17	24.5 (-1.4/+1.5)	40.77	1.32	14.65	10.57	0.26	13.84	11.49	2.45	0.5	0.03	95.87	0.7	0.34	2.5
OD179	g	20	66.3 (-1.8/+1.7)	63.21	0.43	21.75	3.09	0.18	1.13	6.91	1.94	1.06	0.31	86.59	0.39		
	amph	17	33.7 (-1.7/+1.8)	42.05	1.41	15.43	11.54	0.3	13.12	11.19	2.37	0.47	0.12	97.98	0.67	0.32	3.3
OD176	g	21	64.9 (-3.3/+2.2)	64.62	0.34	21.5	2.73	0.17	0.94	6.53	1.85	1.06	0.26	86.77	0.38		
	amph	11	32.1 (-2.3/+1.5)	41.23	1.43	15.98	11.74	0.31	12.79	11.5	2.37	0.47	0.15	97.97	0.66	0.32	4.2
	plag	8	3.0 (-1.3/+2.3)	45.36	BDL	35.35	0.37	BDL	0.02	17.81	1.47	0.03	0.04	100.47			
F241	g	15	100.0	57.66	0.74	19.25	4.48	0.2	4.38	8.06	3.82	1.08	0.32	95.5	0.64		
F242	g	14	62.4 (-4.3/+2.9)	62.68	0.88	18.62	4.91	0.17	1.92	5	3.75	1.62	0.45	94.2	0.41		
	cpx	13	15.7 (-2.2/+2.1)	53.09	0.74	3.14	8.6	0.45	14.12	19.52	0.63	0.06	0.12	100.46	0.75	0.24	
	opx	11	3.7 (-1.1/+1.5)	53.64	0.34	2.29	16.53	0.63	24.62	2.02	0.04	0.02	0.02	100.14	0.73	0.26	
	plag	10	18.2 (-3.2/+3.4)	54.91	0.2	28.09	1.01	0.05	0.34	10.49	4.91	0.24	0.1	100.34			
F245	g	19	55.1 (-4.4/+3.6)	66.96	0.73	17.66	3.95	0.13	1.13	3.74	3.49	1.86	0.34	92.66	0.34		
	cpx	8	18.9 (-2.0/+1.7)	54.33	0.48	2.79	7.53	0.29	14.16	20.32	0.71	0.06	0.06	100.74	0.77	0.15	
	opx	12	5.3 (-1.3/+1.6)	52.04	0.34	2.25	22.91	0.74	20.16	1.95	0.04	BDL	0.02	100.46	0.61	0.33	
	plag	8	20.7 (-3.6/+3.8)	55.14	0.09	28.59	0.59	0.03	0.1	10.28	5.28	0.21	0.05	100.36			

Note: g=glass; ol=olivine; opx=orthopyroxene; cpx=clinopyroxene; plag=plagioclase; amph=amphibole; ap=apatite

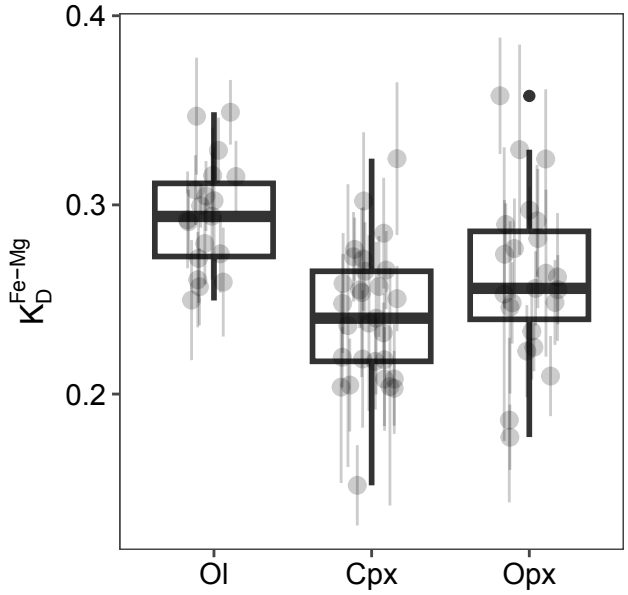

Figure 3: Mineral-melt Fe-Mg K_D for olivine, clinopyroxene, and orthopyroxene. Pale black points are average distribution coefficients for individual experiments; error bars are calculated by analytically propagating standard deviations of the average FeO and MgO of mineral and melt. Jitter around the x-axis is introduced for clarity only. Box and whisker plots show the median (central thick black line), interquartile range (top and bottom of the box), and range of K_D for all experiments.

3.4.3 *Clinopyroxene*

Clinopyroxene composition ranges in Mg# from 75 to 87, and ranges in Al_2O_3 from 0.8 to 5.7 wt.% (Figure 5). On average, clinopyroxene in mixed volatile experiments has higher Al_2O_3 than clinopyroxene in H_2O-saturated experiments. The Fe-Mg K_D for clinopyroxene ranges from 0.15 to 0.32, with a median value of 0.24 (Figure 3; assuming FeO_{tot}). The range of Fe-Mg K_D in our experiments is included within 2 standard deviations of the average clinopyroxene-melt Fe-Mg K_D calculated in Putirka [2008] (0.28 ± 0.16).

3.4.4 *Orthopyroxene*

Orthopyroxene in our experiments is most commonly observed in mixed volatile experiments as a near-liquidus phase, usually with clinopyroxene. Its composition ranges from Mg# 61 to Mg# 87 (where Mg# is calculated Mg / (Mg + Fe_{tot}) all in moles; Figure 5, Table 3). Fe-Mg partitioning between orthopyroxene and melt (assuming FeO_{tot}) ranges from 0.18 to 0.36 with a median value of 0.26 (Figure 3), all of which are within 2 s.d. of the average Fe-Mg K_D calculated by Putirka [2008] (0.29 ± 0.12).

3.4.5 *Plagioclase*

Plagioclase is present in seven of our experiments, six of which were run with mixed volatiles and one of which was run at H_2O-saturated conditions. The composition of the plagioclase ranged from An_{51} to An_{87}. The highest An plagioclase in our experiments crystallized from the H_2O-saturated run, OD176,

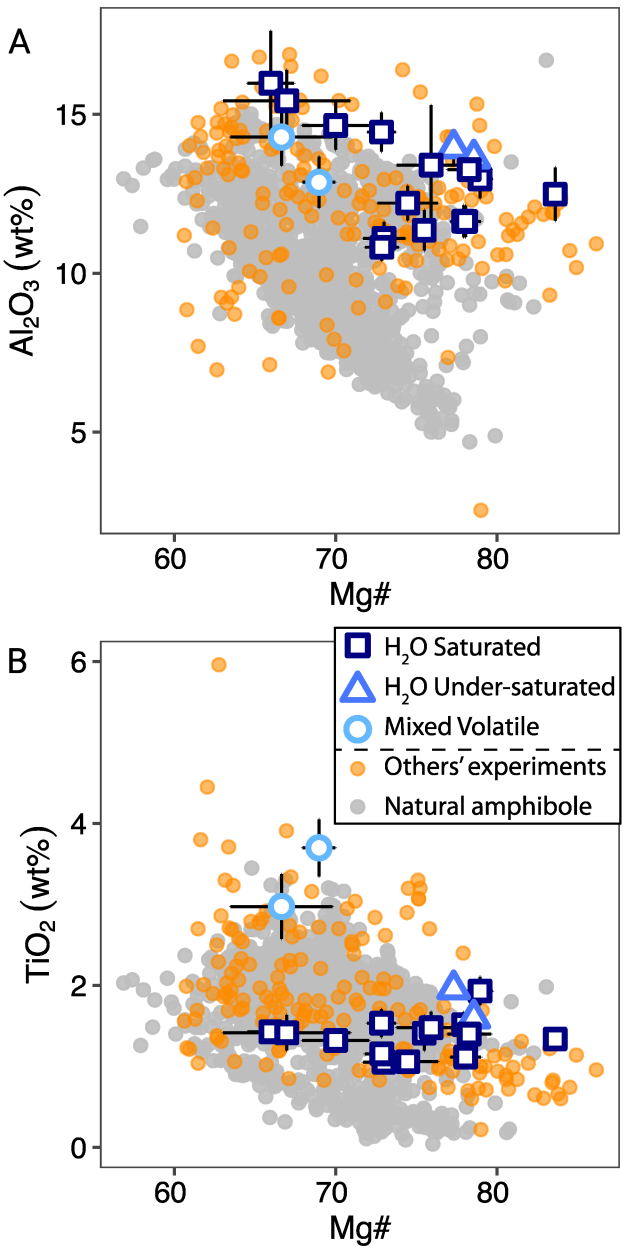

Figure 4: Mg# versus [A] Al_2O_3 and [B] TiO_2 of amphibole in our experiments (blue squares, triangles, and circles), experiments from the literature (orange circles), and in Shiveluch mafic enclaves (grey points). Error bars are 1 standard deviation. The shape and color of our experimental points correspond to the volatile condition of the experiment, as per the legend. Experimental data is from Helz [1976], Sisson and Grove [1993], Kawamoto [1996], Grove et al. [1997], Moore and Carmichael [1998], Martel et al. [1999], Prouteau et al. [1999], Scaillet and Evans [1999], Müntener et al. [2001], Pichavant et al. [2002], Grove et al. [2003], Prouteau and Scaillet [2003], Rutherford [2003], Barclay and Carmichael [2004], Holtz et al. [2005], Sisson et al. [2005], Botcharnikov et al. [2008], Freise et al. [2009], Feig et al. [2010], Krawczynski et al. [2012], Nandedkar et al. [2014], Melekhova et al. [2015], Nandedkar et al. [2016], Andújar et al. [2017], Beermann et al. [2017], Blatter et al. [2017], Pichavant et al. [2018], Ulmer et al. [2018], De Angelis et al. [2020], Marxer et al. [2022], Blatter et al. [2023], and Marxer et al. [2023].

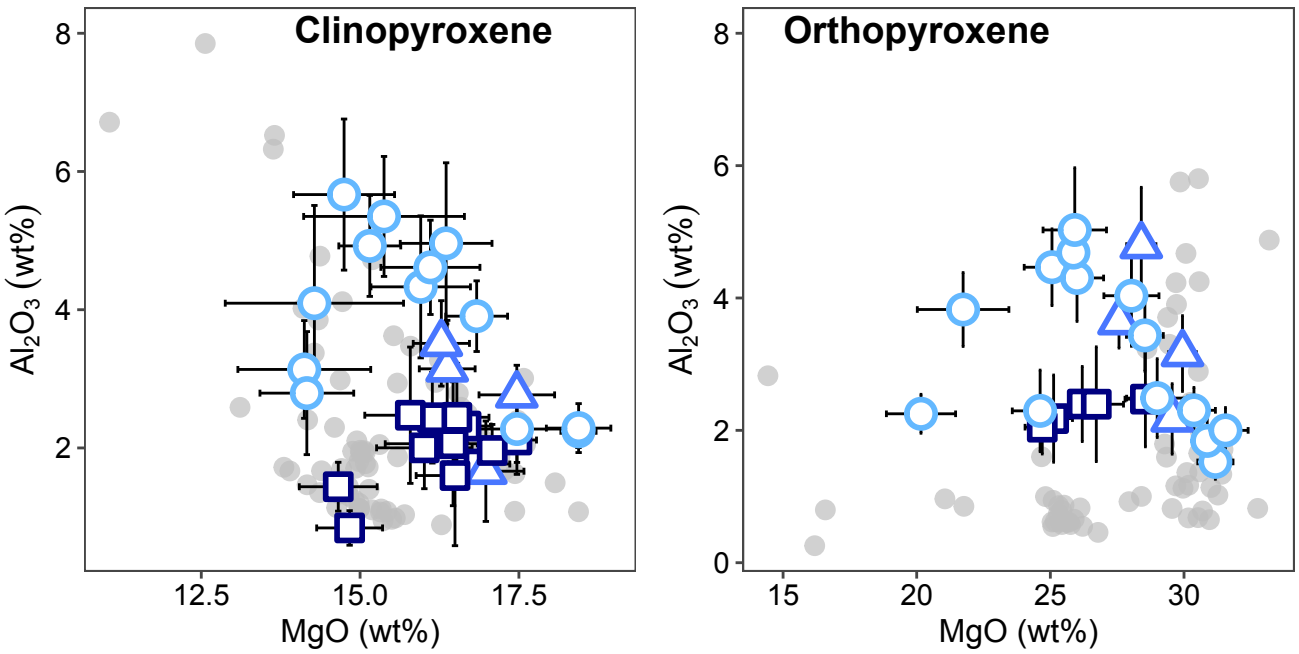

Figure 5: MgO vs Al_2O_3 of clinopyroxene and orthopyroxene in mafic enclaves (grey points) and experiments (blue points). Colors are as in Figure 4. Error bars are 1 standard deviation.

at our lowest experimental temperature, and is in equilibrium with amphibole of Mg# 66. Plagioclase with An_{52-54} is in equilibrium with amphibole (Mg# 67-69) in mixed volatile experiments.

3.4.6 *Glass*

Glasses generally decrease in CaO and FeO_{tot} and increase in SiO_2 and K_2O with decreasing MgO, and there is significant overlap in the CaO, FeO_{tot}, K_2O, and SiO_2 contents of glasses in mixed volatile, H_2O-undersaturated, and H_2O-saturated experiments (Figure 6, Supplementary Material [Goltz 2026] Figure S2). In H_2O-saturated experiments, FeO_{tot} appears to plateau until around 3 wt.% MgO, at which point amphibole crystallization drives a decrease in FeO_{tot}, as has also been observed in other experimental studies [Andrys et al. 2024]. In contrast, FeO_{tot} consistently decreases in mixed-volatile experiments, even without the crystallization of amphibole or magnetite, due to crystallization of orthopyroxene high in FeO relative to the melt (Table 3); as a result, we do not discuss FeO_{tot} as a good discriminant between melts with different volatile contents. On the other hand, glasses from amphibole-bearing H_2O-saturated experiments decrease in TiO_2 around 4 wt.% MgO or lower; glasses from mixed volatile experiments maintain a constant TiO_2 with relatively low MgO and are higher in TiO_2 than glasses from H_2O-saturated experiments at the same MgO, regardless of the presence or absence of amphibole in the charge. Glasses in several mixed volatile experiments are lower in Al_2O_3 than H_2O-saturated experiments at the same MgO, which may be related to the presence of plagioclase in these experimental charges. Glasses in our H_2O-saturated experiments are low in alkalis relative to glasses from mixed volatile experiments, likely due to the preferential partitioning of these fluid-mobile elements into a free fluid phase.

4 Discussion

The primary goal of this study is to put constraints on the processes controlling the chemical evolution of the crustal magma system at Shiveluch Volcano, Kamchatka. We have conducted a suite of 47 high-pressure experiments on two primitive magmas erupted at Shiveluch and their derivatives. In order to draw conclusions, we directly compare the phase assemblages and phase compositions of our experiments to the whole rock compositions, phase assemblages, and phase compositions of basaltic tephra, mafic enclaves, and andesites erupted at Shiveluch. We find that the generation of andesites at Shiveluch requires some high-pressure differentiation of variably hydrated basalts in addition to other processes.

4.1 Conditions of mid-to-lower crustal storage at Shiveluch

Our approach in using experiments to constrain the conditions of mid to lower crustal crystallization at Shiveluch is similar to the approach used to determine the conditions of shallow intermediate magma storage prior to explosive eruptions at volcanoes like Mt. St. Helens, Pinatubo, Santorini, Volcan Colima, Mascota, and Novarupta [e.g. Rutherford et al. 1985; Rutherford and Devine 1996; Moore and Carmichael 1998; Cottrell et al. 1999; Hammer et al. 2002; Prouteau and Scaillet 2003]. In those studies, P-T-X_{H_2O} space was mapped for erupted compositions. The likely P-T-X_{H_2O} of crystallization was determined by matching the observed phase assemblage in the erupted products to an area in the resulting phase diagram. Results were further refined and models given more complexity using phase chemistry, particularly of amphibole

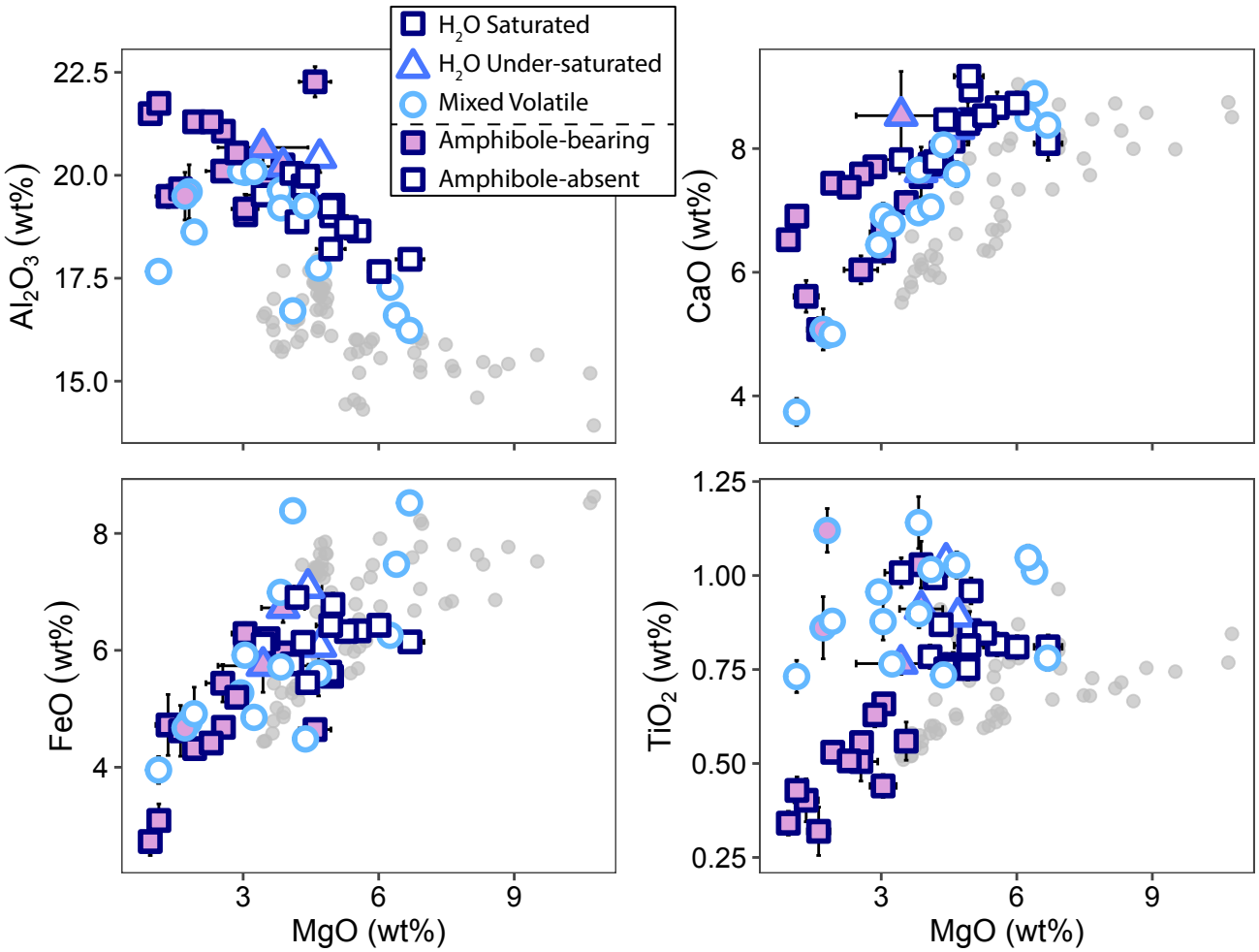

Figure 6: Compositional variation diagrams of experimental glasses and natural samples from Shiveluch. The color and shape of open shapes refers to the volatile content of the experiment containing that amphibole: dark blue squares are water saturated, periwinkle triangles are water undersaturated, and light blue circles are mixed volatiles. Points filled with pink represent experimental glasses in equilibrium with amphibole. Grey points are whole rock compositions of tephra, mafic enclaves, and andesites erupted from Shiveluch from Hochstaedter et al. [1996], Ishikawa et al. [2001], Ponomareva et al. [2007], Ferlito [2011], Gorbach and Portnyagin [2011], and Goltz et al. [2020].

[e.g. Rutherford and Devine 1988; Prouteau and Scaillet 2003]. These experiments were crucial, especially to relate the location of earthquakes to depths of shallow storage within the crust [e.g. Rutherford et al. 1985]. Since then, the importance of lower crustal processes to volcanic behavior has been emphasized by models [e.g. Annen et al. 2006; Karakas et al. 2017; Glazner 2021] and petrographic and geochemical observations [e.g. Davidson et al. 2007; Burns and de Silva 2023]. The lower crust is a fruitful area for study experimentally [e.g. Melekhova et al. 2015; Ulmer et al. 2018], and we explore lower crustal storage here in the context of Shiveluch, where mafic enclaves preserve near-liquidus phase assemblages and relatively undifferentiated magmatic compositions [Goltz et al. 2020]. In the case of the Shiveluch mafic enclaves, the target mineral assemblage is amphibole + olivine ± clinopyroxene. This is the near-liquidus assemblage in mafic enclaves and tephra, and minerals are accordingly high Mg# (ol ≥ Fo_{88}, amph ≥ Mg# 70, cpx Mg# ≥ 80). In mafic enclaves, some amphibole with high Mg# (i.e. Mg# ≥ 74) is found as inclusions in high forsterite (Fo > 88) olivine [Goltz et al. 2020].

The target assemblage (amph + ol ± cpx) is relatively rare in the experimental literature. This may be partially related to the peritectic reaction of olivine ± pyroxenes to produce amphibole. Due to the peritectic reaction, inverse experiments (i.e. those where the peritectic liquid is used as the starting composition) may not crystallize the reactant mineral assemblage, meaning that even experiments conducted at relevant *P-T* conditions may not have the co-existing olivine and amphibole that we target here. We used a compilation of phase equilibrium experiments from Weber and Blundy [2024] to identify experiments containing equilibrium amphibole and olivine and compare them to our experimental products. The database of Weber and Blundy [2024] includes a summary of phase assemblages and published glass compositions normalized to 100. From a database of 2,546 experiments, only 74 experiments contain the key assemblage of amphibole +

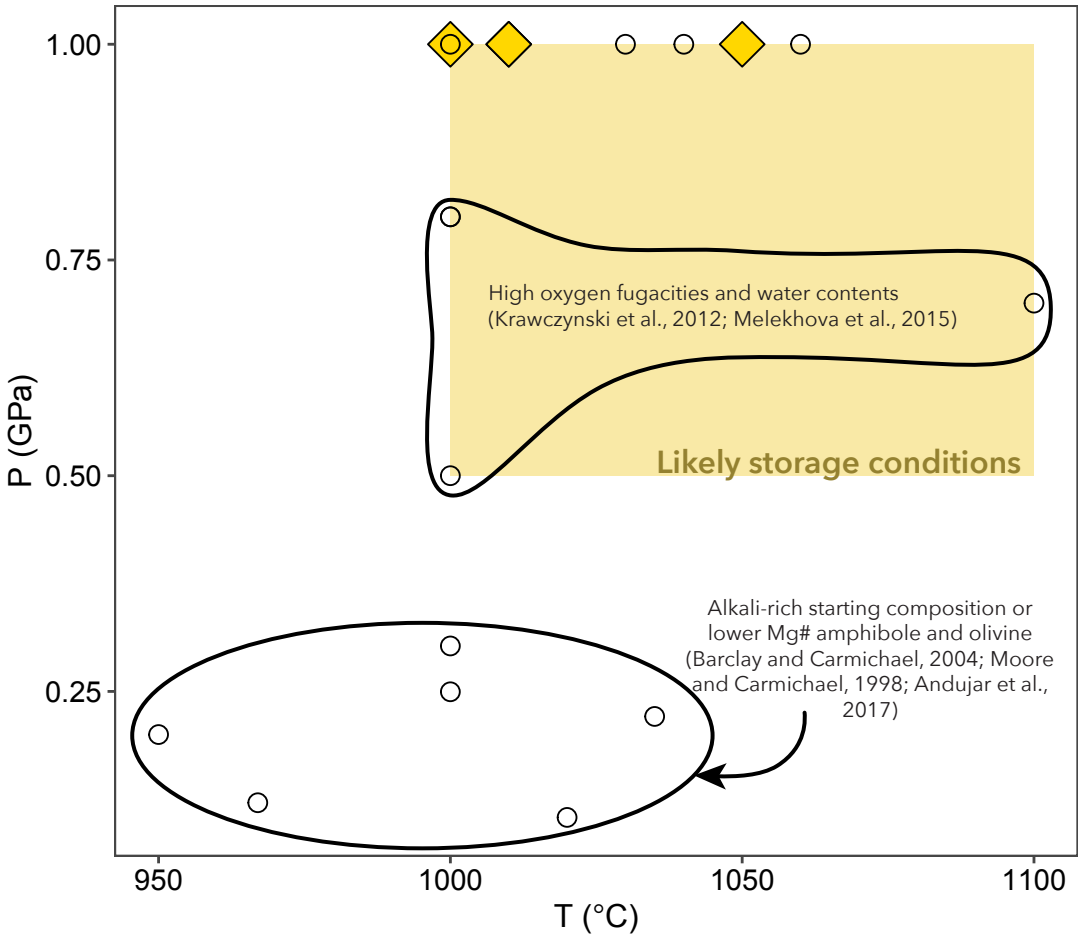

Figure 7: Pressure and temperature conditions of experiments with amphibole and olivine from this study (yellow diamonds) and the literature (open black circles). See Table 4 for more details on compiled amphibole- and olivine-bearing experiments from the literature.

olivine (Supplementary Material [Goltz 2026] Table S4). To these, we manually added published compositional information for clinopyroxene, olivine and amphibole where available; this compilation is available in Supplementary Material [Goltz 2026] Table S4. Of the 74 experiments, 50 % have plagioclase in their equilibrium assemblage, which is dissimilar to our target assemblage, and thus we do not discuss them further. All but one of the plagioclase-bearing experiments equilibrated at relatively low temperatures at or below 1000 °C and at or below 700 MPa. Of the 37 remaining plagioclase-free experiments, we exclude from discussion 10 additional experiments from Kelemen et al. [1990] and 7 experiments from Helz [1976] because amphibole in those experiments was crystallized during the quench of the experiment. We also exclude an additional 6 experiments from Prouteau and Scaillet [2003]; these experiments, designed to assess the equilibrium between dacite and peridotite, only achieved localized equilibrium, as evidenced by heterogeneity in crystal chemistry and the presence of reaction rims around olivine crystals.

The remaining 20 plagioclase-free experiments provide an interesting window to the factors controlling amphibole stability in hydrous melts (Figure 7, Table 4). For example, experiments at upper crustal pressures (i.e. ≤ 300 MPa) where high Mg# amphibole and olivine are in equilibrium with mafic melt are from a higher alkali region of compositional space (Na_2O of basaltic starting compositions ranges from 3.97 to 4.59 wt.%; Moore and Carmichael [1998] and Barclay and Carmichael [2004]); enrichment in alkalis promotes amphibole stability at higher temperatures [Wallace and Green 1991; Mandler and Grove 2016], which likely contributed to the near-liquidus amphibole crystallization in these experiments. At mid-crustal pressures (300–700 MPa), high oxygen fugacities (up to NNO+5) increased the liquidus temperature of amphibole, allowing it to be in equilibrium with high Mg# olivine [e.g. Krawczynski et al. 2012; Melekhova et al. 2015]. At higher pressures, the effect of H_2O content is evident; all experiments with amphibole at 1 GPa are H_2O saturated (likely water contents > 10 wt.%, and potentially up to 20 wt.%; Mitchell et al. [2017]), with the exception of experiment BM24 [Melekhova et al. 2015], which has a melt H_2O content of 9.3 wt.%.

Our experiments—which show that amphibole and olivine are stable between 1000 and 1050 °C at 1 GPa and H_2O saturated conditions (Table 2, Figure 7)—align well with the conditions of amphibole + olivine stability demonstrated in the

Table 4: Details of experiments with equilibrium amphibole + olivine from the compilation of Weber and Blundy [2024].

Study	Experiment IDs	T (°C)	P (GPa)	fO_2	H_2O (in glass)	Mineral Assemblage	Starting Composition
Barclay and Carmichael [2004]	Jor46.10, Jor46.31, Jor46.21	967–1035	0.104–0.221	NNO+1.3–NNO+2	3.5–5.4 wt.%	ol + cpx + amph + bt + sp + ap	ne-normative trachybasalt (Cerro la Pilita, TMVB)
Moore and Carmichael [1998]	PEM22-20, PEM22-19	1000	0.250–0.303	~NNO+1–NNO+2	5.8–6.4 wt.%	ol + amph ± aug	basaltic andesite (Mascota, TMVB)
Andújar et al. [2017]	T6	950	0.2	NNO+1	6.05 wt.%	ol + cpx + mt + amph	andesite (Tungurahua, Ecuador, Andean NVZ)
Krawczynski et al. [2012]	B1133, B1160, 44-102	1000	0.5–0.8	NNO–NNO+3	Saturated (~9–12 wt.%)	ol + cpx + amph ± opx ± mt	magnesian andesite (85-41c) and basaltic andesite (85-44) (Mt. Shasta, Cascades)
Melekhova et al. [2015]	BM34, BM24	1030–1100	0.7–1	NNO+1.8–NNO+5.0	7.2–9.3 wt.%	ol + cpx + amph + sp ± quench crystals	basalt (St. Vincent, Lesser Antilles)
Ulmer et al. [2018]	P1060, PU905, PU1005	1000–1060	1	CCOH–NNO+5.5	6.7–9 wt.%	ol + cpx + opx + amph + sp	high Mg# basalt (southern Adamello batholith)

literature, despite having different starting compositions and being run at a different oxygen fugacity. Taking into consideration our experimental results and published results from experiments with broadly similar bulk compositions, conducted at oxygen fugacities ranging C-COH to NNO+5.5 [Krawczynski et al. 2012; Melekhova et al. 2015; Ulmer et al. 2018], we bracket the conditions of high Mg# olivine and amphibole crystallization from mafic magmas at Shiveluch between 500 MPa and 1 GPa, and from 1000–1100 °C, with high (≥ 7.2 wt.%) H_2O contents and at a range of oxygen fugacities. These conditions align with those estimated by microanalysis of minerals in mafic enclaves by Goltz et al. [2020].

The agreement between our experiments and results from the literature gives us confidence in and adds nuance to our results while exposing a fundamental problem with the experimental approach to creating new phase diagrams. Namely, there is no way to predict the extent to which we can accurately extrapolate between phase diagrams with multidimensional compositional differences in the presence of amphibole because of the inability of current models to predict amphibole stability. A question we must address in coming years is: how similar is similar enough when we consider the effect of variations in compositional space on phase stability and composition? A combination of experimental and modeling efforts is required to constrain and fill gaps in the experimental literature through which extrapolation cannot be done accurately.

4.2 Processes contributing to the generation of andesite at Shiveluch

Below, we compare mineral and melt compositions in our experiments to those observed in natural samples to elucidate the processes contributing to andesite genesis at Shiveluch.

4.2.1 *Fractional crystallization plays a role in generating andesite*

The fractionation of phases crystallized in equilibrium with superhydrous magmas produces similar trends in major element oxides defined by andesites and mafic enclaves (with a noticeable exception of Al_2O_3, discussed below, and the experiments having a slightly higher CaO content) extending to lower MgO (Figure 6). Specifically, we find that glass compositions in H_2O-saturated experiments that bear amphibole best reproduce the chemical trends in TiO_2 defined by whole rock compositions of andesites and mafic enclaves. While experiments reproduce the observed decrease in TiO_2 with decreasing MgO, they extend the trend to lower MgO, and have limited overlap with the compositions of natural samples. This may be related to a delay in amphibole saturation in the experiments caused by alkali-loss to excess fluids (see Section 2). In their study of mafic enclaves, Goltz et al. [2020] interpreted decreases in whole-rock TiO_2 and CaO with decreasing MgO starting at MgO ~4 wt.% as resulting from increased amphibole fractionation leading to compatible behavior of TiO_2.

Decreasing melt TiO_2 could be attributed to a change in the partitioning behavior of titanium between amphibole and melt or to the fractionation of more amphibole relative to other phases. We calculated the partition coefficient of titanium between amphibole and melt (D_{Ti}) for all amphibole-bearing

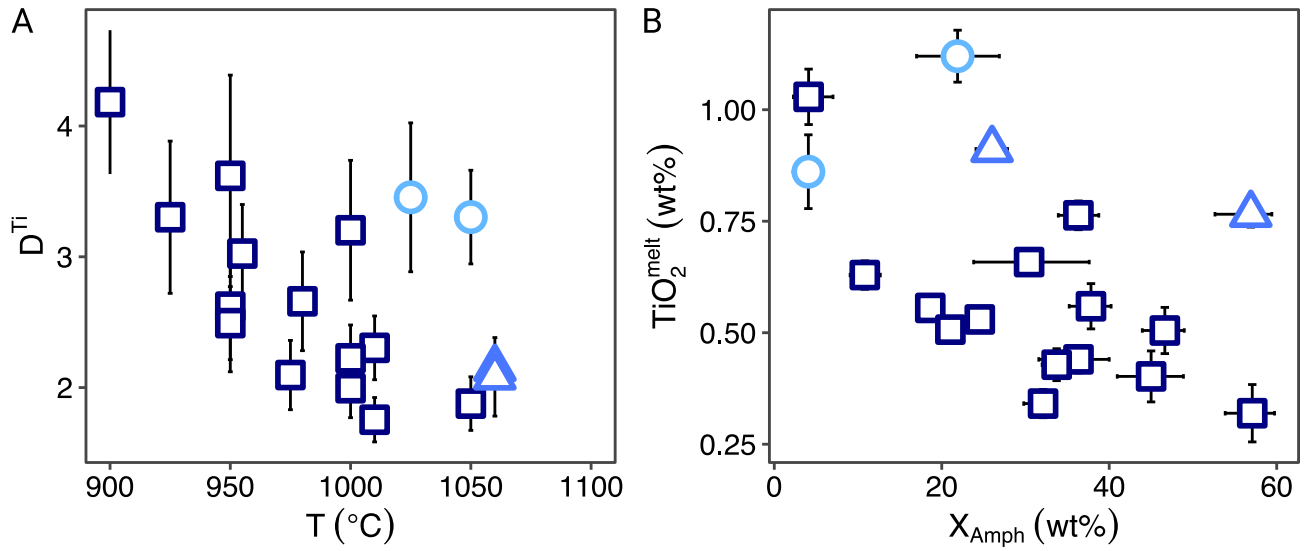

Figure 8: [A] Titanium partitioning between amphibole and melt (D_{Ti}) as a function of temperature. [B] Titanium content of experimental melt (TiO_{melt}) as a function of the proportion of amphibole in the experiment (X_{amph}). Colors and symbols are as in Figure 4

experiments without normalizing amphibole compositions to 100 (Figure 8). On average, the partition coefficient of titanium between amphibole and melt in our experiments is 2.7 ± 0.7, consistent with partition coefficients from Waters et al. [2021] and Andrys et al. [2024]. The partition coefficient is only weakly correlated with experimental temperature, as was also reported in Ulmer et al. [2018]. The lowest H_2O content experiments containing amphibole do have the highest titanium content among amphiboles crystallized in this study by at least 1–2 weight percent (Figure 4b, Table 3), but the amphibole-melt titanium partition coefficients (3.3 and 3.5) are within 2 standard deviations of the average value. To summarize, the decrease in titanium observed in H_2O-saturated experiments containing amphibole is not associated with changes to the amphibole-melt titanium partition coefficient as a function of temperature (Figure 8). The trend in decreasing titanium observed in natural whole rock compositions thus indicates a necessary increase of amphibole percent in fractionated solids (see Figure 8b), in the absence of titanium-rich phases like ilmenite or Ti-rich magnetite, for which there is no petrographic evidence for early crystallization [Goltz et al. 2020].

The high proportion of amphibole in H_2O-saturated experiments causes experimental glasses in these experiments to decrease in TiO_2 with decreasing Mg#, as has also been proposed in Nandedkar et al. [2014], Ulmer et al. [2018], Waters et al. [2021], Marxer et al. [2022, 2023], and Andrys et al. [2024]. The titanium content of the melt is negatively correlated with the percent of amphibole in the experiment among amphibole-bearing experiments (Figure 8). The implication of this finding is that the titanium content of a melt in equilibrium with a high proportion of amphibole will decrease. In our experiments, such high proportions of amphibole (i.e. ≫ 20 %) only crystallize in experiments with very high (i.e. ≥ 10 wt.%) H_2O contents, which indicates the importance of superhydrous melts in the liquid line of descent and the production of andesite at Shiveluch.

4.2.2 *Crustal melting also contributes to the generation of andesites at Shiveluch*

Although glasses in H_2O-saturated experiments reproduce the trend of decreasing TiO_2 observed in natural samples, glasses are much higher in Al_2O_3 than natural andesites and are slightly higher in CaO (Figure 6). The enrichment of Al_2O_3 in glass synthesized from hydrous, high pressure experiments relative to andesites and dacites has been observed by others [e.g. Blatter et al. 2013; 2017; Marxer et al. 2022; Blatter et al. 2023; Marxer et al. 2023] and is caused by the suppression of plagioclase at high H_2O contents [Sisson and Grove 1993]. While hydrous crystallization of basalt at upper crustal pressures (i.e. 100–200 MPa) produces glasses more similar in Al_2O_3 to natural andesites and dacites [e.g. Rutherford et al. 1985; Barclay and Carmichael 2004; McCanta et al. 2007], these experiments do not produce the high Mg# amphibole and olivine assemblage from lower alkali content basalt that we observe in mafic enclaves, and thus this mechanism cannot work alone to produce intermediate arc lavas.

Others have invoked mixing in the upper and lower crust, crustal melting, and polybaric crystallization pathways to reconcile the high Al_2O_3 experimental melts with relatively low Al_2O_3 whole rock compositions, with various implications for crustal growth and delamination [Blatter et al. 2017; Rezeau et al. 2021; Marxer et al. 2022; Blatter et al. 2023; Marxer et al. 2023; Andrys et al. 2024]. The compositions of amphibole in mafic enclaves and experiments can help refine this list of hypotheses.

Generally, we find that the compositions of minerals in our experiments are similar to compositions observed in mafic enclaves (Figure 5). An important exception is the composition of amphiboles. At Mg# greater than ~70, amphiboles in Shiv-

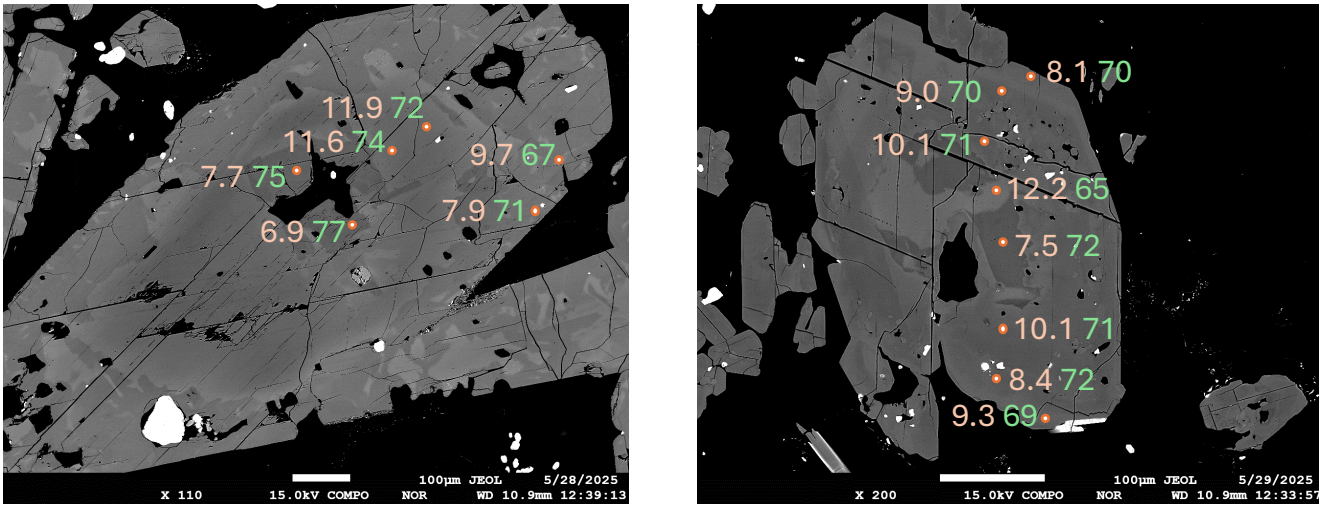

Figure 9: Back-scatter electron (BSE) images of amphiboles from samples 17-15f and 17-02B of Goltz et al. [2020]. The aluminum content and Mg# of the analyzed points (shown as white points with orange stroke) is shown in orange and green text, respectively. Images and data were collected at Carnegie Science; see Supplementary Material [Goltz 2026] for details on microprobe analyses and Table S6 for complete microprobe data.

eluch mafic enclaves seem to define two groups: one with relatively high Al_2O_3 (11–12 wt.%) and one with relatively low Al_2O_3 (< 10 wt.%) (Figure 4). The groups converge at lower Mg# and higher Al_2O_3. At these Mg#, amphiboles in our experiments only overlap with the higher Al_2O_3 group. Similarly low Al_2O_3, high Mg# amphiboles have also been observed at Mt. Shasta [Krawczynski 2011], Ciomadul [Cserép et al. 2023], Buldir [Waters et al. 2021], and Mt. Pinatubo [Bernard et al. 1996; Rutherford and Devine 1996].

In the mafic enclaves, low Al_2O_3, high Mg# amphiboles are observed in a variety of contexts. In addition to being observed at the rims of amphiboles with relatively high Al_2O_3, they are found in complex zoning relationships with higher Al_2O_3, high Mg# amphiboles (Figure 9). In Figure 9, high Mg#, low Al_2O_3 amphiboles are both in the core and at the rim of amphibole phenocrysts with higher Al_2O_3. The petrologic context of the low Al_2O_3 amphiboles is key to their interpretation, as we will expand upon below.

One possibility to produce the low Al_2O_3, high Mg# amphiboles is polybaric crystallization of basalt. The Al-Tschermak's exchange in amphibole is widely recognized as a thermodynamic barometer for relatively silicic melts [Blundy and Holland 1990]. For less silicic melts, ^{VI}Al of amphibole has been empirically calibrated as a barometer [e.g. Larocque and Canil 2010; Ridolfi et al. 2010; Krawczynski et al. 2012]. Generally, amphibole crystallized at lower pressure should have lower ^{VI}Al than an amphibole crystallized at higher pressures from a melt of identical composition. A few observations suggest that lower pressure crystallization alone cannot explain the high Mg#, low Al_2O_3 amphiboles in the mafic enclaves. First, there is extremely limited overlap between the composition of amphiboles in the experimental literature—including experiments run at relatively low and high pressures and at a range of starting compositions—and the low Al_2O_3, high Mg# amphiboles we observe (Figure 4a). Excepting experiments from Nandedkar et al. [2014, 2016] which contain extremely MnO-rich amphiboles (i.e. 0.8–3.4 wt.%; for context, typical amphiboles in our database have 0.1–0.4 wt.% MnO), experiments closest in composition to the group of low Al_2O_3, high Mg# amphiboles that we observe in the mafic enclaves were done at low pressures (~200 MPa) with a dacitic starting composition, and are relatively crystalline [Scaillet and Evans 1999]. Second, the observation of high Mg#, low Al_2O_3 amphiboles in the cores of some otherwise relatively high Al_2O_3 amphiboles (Figure 9) shows that a population of low Al_2O_3 amphiboles may have crystallized before high Al_2O_3 amphibole (though alternative explanations for this observation are possible; see below). If the aluminum content of the amphiboles was strictly related to pressure, this would require low and then subsequent high pressure crystallization of amphibole, which is unlikely, given the neutral to positive buoyancy of magma in the crust.

The low Al_2O_3, high Mg# cores thus require a more nuanced explanation beyond polybaric crystallization. One alternative interpretation of the low Al_2O_3, high Mg# cores is that they formed during magmatic ascent. This interpretation rests on the interpretation of the texture of the low Al_2O_3, high Mg# amphibole cores as resorbed and is supported by the similarity in Al_2O_3 of cores to amphibole rims, which may have feasibly crystallized at lower pressures. In this scenario, interconnected embayments in 3D would have connected the amphibole to the equilibrium melt. This is not our preferred explanation, however, because if this were the dominant mechanism for producing this population of amphibole cores, then the cores should be similar not only in Al_2O_3 but also in Mg# to rims; this is not always the case, as evidenced by the difference in Mg# between cores and rims in Figure 9a.

If the cores are indeed resorbed, another interpretation may be that the low Al_2O_3, high Mg# cores are xenocrystic and inherited from a metasomatized ultramafic lithology. Amphibole in subarc, metasomatized ultramafic lithologies tends to be low in Al_2O_3 and high in Mg# [e.g. Prouteau et al. 2001;

Cserép et al. 2023]; indeed, high Mg#, low Al_2O_3 amphiboles have been observed in upper mantle xenoliths from Shiveluch [Bryant et al. 2007]. It is possible that the low Al_2O_3, high Mg# cores that we observe in the enclaves are relict from these upper mantle lithologies or perhaps formed as a consequence of melt-peridotite interaction in the uppermost mantle.

Both of these hypotheses to explain the low Al_2O_3, high Mg# amphibole cores rely on the interpretation of the cores' texture as indicative of resorption. This is not necessarily the case. Primary growth textures run the gamut from euhedral to relatively wormy because of skeletal or dendritic growth patterns caused by high degrees of undercooling or, potentially, low magmatic H_2O contents [e.g. Shea and Hammer 2013; Welsch et al. 2013; Erdmann et al. 2014; Masotta et al. 2020]. Thus, the wormy textures of low Al_2O_3, high Mg# cores could be related to a period of primary dendritic growth, rather than to secondary resorption.

Our preferred mechanism interprets the low Al_2O_3, high Mg# as resulting from primary crystallization from a relatively SiO_2-rich, metaluminous magma. Low Al_2O_3 amphiboles are correspondingly high in SiO_2 to fill the tetrahedrally-coordinated site in the amphibole structure (i.e. T site; Hawthorne and Oberti [2007]) and so may be more likely to crystallize from a relatively high SiO_2 melt. The low Al_2O_3 of a metaluminous magma (relative to the peraluminous intermediate melts produced via fractional crystallization of basalt) may encourage crystallization of a relatively low Al_2O_3 amphibole, even at high pressures [e.g. Larocque and Canil 2010; Krawczynski et al. 2012; Putirka 2016]. Intermediate (i.e. relatively high SiO_2, potentially dacitic), metaluminous magmas could be produced via peritectic melting of an existing assemblage of 2-pyroxenes + amphibole ± plagioclase [Blatter et al. 2017] in the mid-to-lower crust. While there is no robust regional seismic model of the crust underlying Shiveluch, a study of the more southerly Klyushevskoy group volcanoes shows that the lowermost 10 km of the crust is basaltic [Fedotov et al. 2010]. If this crustal structure extends below Shiveluch, it is possible that the mafic lower crust could melt to produce lower Al_2O_3, higher SiO_2 magmas, a process that does not require the presence of garnet [Blatter et al. 2017]. Subsequent mixing with basalt (as proposed in Blatter et al. [2023]) is a mechanism that could produce both low Al_2O_3, high Mg# amphibole and metaluminous andesite at Shiveluch. While we cannot discount the possibility that all low-Al_2O_3, high Mg# amphibole cores are amphibole xenocrysts, our preferred explanation involves crustal melting and primary crystallization, which can account for both the chemistry of the amphibole and generate metaluminous magmas. This hypothetical mechanism to produce low Al_2O_3, high Mg# amphibole and metaluminous intermediate melts may be tested in the future by microanalyzing trace elements in high Mg# amphibole with variable Al_2O_3 and with further experimentation.

5 Conclusions

Our experiments show that mid-to-lower crustal differentiation of a hydrous basalt is required to reproduce the near liquidus phase assemblage of amphibole + olivine ± clinopyroxene observed in mafic enclaves at Shiveluch. We find that primitive magmas likely equilibrated with the observed near-liquidus assemblage between 500 MPa and 1 GPa, and from 1000–1100 °C, with high (≥ 7.2 wt.%) H_2O contents, consistent with mineral geobarometry and thermometry [Goltz et al. 2020]. However, this process cannot produce the metaluminous andesite erupted at Shiveluch and a group of low Al_2O_3, high Mg# amphibole alone. Using experimental data from the literature, we suggest that crystallization of and mixing of basalt with a hydrous dacite produced by melting of existing crust is also a key process in andesite production.

Author Contributions

A.E.G. conducted and analyzed experiments, synthesized data, compiled relevant literature data, and wrote and edited this manuscript. M.J.K. initially conceptualized this study, aided in data analysis, and edited the manuscript.

Acknowledgements

A.E.G. thanks Kelsey Prissel and Helene Couvy for their mentorship in and outside of the lab, and Paul Carpenter and Emma Bullock for their help with probe analyses (WashU and Carnegie, respectively), enthusiasm, and re-assurance that everything would indeed be "awesome". A.E.G. acknowledges funding from the McDonnell Center for the Space Sciences at Washington University in St. Louis and from Carnegie Science. M.J.K. and A.E.G. acknowledge funding from NSF EAR grant #2042386 and M.J.K. acknowledges funding from NSF EAR grant #2047960. Both authors thank Felix Marxer, Janine Andrys, and Etienne Medard for exceptionally constructive reviews which strengthened the quality of this manuscript, and thank Martin Mangler for editorial handling.

Data Availability

Computer-readable data for this manuscript is freely available at `https://github.com/aegoltz/Goltz-and-Krawczynski-Supplementary-Data`, archived via Zenodo at 10.5281/zenodo.21775680 [Goltz 2026].

Copyright Notice

References

Andrys, J. L., E. Cottrell, K. A. Kelley, L. E. Waters, and M. L. Coombs (2024). "Insights on Arc Magmatic Systems Drawn from Natural Melt Inclusions and Crystallization Experiments at P_{H_2O} = 800 MPa under Oxidizing Conditions". *Journal of Petrology* 65(12). DOI: 10.1093/petrology/egae117.

Andújar, J., C. Martel, M. Pichavant, P. Samaniego, B. Scaillet, and I. Molina (2017). "Structure of the Plumbing System at Tungurahua Volcano, Ecuador: Insights from Phase Equilibrium Experiments on July–August 2006 Eruption Prod-

ucts". *Journal of Petrology* 58(7), pages 1249–1278. DOI: 10.1093/petrology/egx054.

Annen, C., J. D. Blundy, and R. S. J. Sparks (2006). "The Genesis of Intermediate and Silicic Magmas in Deep Crustal Hot Zones". *Journal of Petrology* 47(3), pages 505–539. DOI: 10.1093/petrology/egi084.

Bacon, C. R. (1986). "Magmatic inclusions in silicic and intermediate volcanic rocks". *Journal of Geophysical Research: Solid Earth* 91(B6), pages 6091–6112. DOI: 10.1029/jb091ib06p06091.

Balta, J. B., J. R. Beckett, and P. D. Asimow (2011). "Thermodynamic properties of alloys of gold-74/palladium-26 with variable amounts of iron and the use of Au-Pd-Fe alloys as containers for experimental petrology". *American Mineralogist* 96(10), pages 1467–1474. DOI: 10.2138/am.2011.3637.

Barclay, J. and I. Carmichael (2004). "A Hornblende Basalt from Western Mexico: Water-saturated Phase Relations Constrain a Pressure-Temperature Window of Eruptibility". *Journal of Petrology* 45(3), pages 485–506. DOI: 10.1093/petrology/egg091.

Barth, A., M. Portnyagin, N. Mironov, F. Holtz, Y. Moussallam, E. F. Rose-Koga, D. Rasmussen, H. Towbin, H. Gonnermann, E. J. Mutch, S. G. Rotolo, and T. Plank (2024). "Fast, furious, and gassy: Etna's explosive eruption from the mantle". *Earth and Planetary Science Letters* 643, page 118864. DOI: 10.1016/j.epsl.2024.118864.

Beermann, O., F. Holtz, and E. Duesterhoeft (2017). "Magma storage conditions and differentiation of the mafic Lower Pollara volcanics, Salina Island, Aeolian Islands, Italy: implications for the formation conditions of shoshonites and potassic rocks". *Contributions to Mineralogy and Petrology* 172(5). DOI: 10.1007/s00410-017-1363-z.

Bernard, A., U. Knittel, B. Weber, D. Weis, A. Albrecht, K. Hattori, J. Klein, and D. Oles (1996). "Petrology and geochemistry of the 1991 eruption products of Mount Pinatubo". *Fire and Mud: Eruptions and Lahars of Mount Pinatubo, Philippines*. Edited by C. Newhall and S. Raymundo. University of Washington Press, pages 767–797. ISBN: 9780295975856.

Blatter, D. L., T. W. Sisson, and W. B. Hankins (2013). "Crystallization of oxidized, moderately hydrous arc basalt at mid- to lower-crustal pressures: implications for andesite genesis". *Contributions to Mineralogy and Petrology* 166(3), pages 861–886. DOI: 10.1007/s00410-013-0920-3.

– (2017). "Voluminous arc dacites as amphibole reaction-boundary liquids". *Contributions to Mineralogy and Petrology* 172(5). DOI: 10.1007/s00410-017-1340-6.

– (2023). "Garnet stability in arc basalt, andesite, and dacite—an experimental study". *Contributions to Mineralogy and Petrology* 178(6). DOI: 10.1007/s00410-023-02008-w.

Blundy, J. D. and T. J. B. Holland (1990). "Calcic amphibole equilibria and a new amphibole-plagioclase geothermometer". *Contributions to Mineralogy and Petrology* 104(2), pages 208–224. DOI: 10.1007/bf00306444.

Botcharnikov, R. E., F. Holtz, R. R. Almeev, H. Sato, and H. Behrens (2008). "Storage conditions and evolution of andesitic magma prior to the 1991–95 eruption of Unzen volcano: Constraints from natural samples and phase equilibria experiments". *Journal of Volcanology and Geothermal Research* 175(1-2), pages 168–180. DOI: 10.1016/j.jvolgeores.2008.03.026.

Bryant, J. A., G. M. Yogodzinski, and T. G. Churikova (2007). "Melt-mantle interactions beneath the Kamchatka arc: Evidence from ultramafic xenoliths from Shiveluch volcano". *Geochemistry, Geophysics, Geosystems* 8(4). DOI: 10.1029/2006gc001443.

Burns, D. H. and S. L. de Silva (2023). "Andesites and evolution of the continental crust: Perspectives from the Central Volcanic Zone of the Andes". *Frontiers in Earth Science* 10. DOI: 10.3389/feart.2022.961130.

Cottrell, E., J. E. Gardner, and M. J. Rutherford (1999). "Petrologic and experimental evidence for the movement and heating of the pre-eruptive Minoan rhyodacite (Santorini, Greece)". *Contributions to Mineralogy and Petrology* 135(4), pages 315–331. DOI: 10.1007/s004100050514.

Cserép, B., M. Szemerédi, S. Harangi, S. Erdmann, O. Bachmann, I. Dunkl, I. Seghedi, K. Mészáros, Z. Kovács, A. Virág, T. Ntaflos, D. Schiller, K. Molnár, and R. Lukács (2023). "Constraints on the pre-eruptive magma storage conditions and magma evolution of the 56–30 ka explosive volcanism of Ciomadul (East Carpathians, Romania)". *Contributions to Mineralogy and Petrology* 178(12). DOI: 10.1007/s00410-023-02075-z.

Davidson, J., S. Turner, H. Handley, C. Macpherson, and A. Dosseto (2007). "Amphibole "sponge" in arc crust?" *Geology* 35(9), page 787. DOI: 10.1130/g23637a.1.

Davidson, J., S. Turner, and T. Plank (2013). "Dy/Dy*: Variations Arising from Mantle Sources and Petrogenetic Processes". *Journal of Petrology* 54(3), pages 525–537. DOI: 10.1093/petrology/egs076.

Dayton, K., E. Gazel, P. Wieser, V. R. Troll, J. C. Carracedo, H. La Madrid, D. C. Roman, J. Ward, M. Aulinas, H. Geiger, F. M. Deegan, G. Gisbert, and F. J. Perez-Torrado (2023). "Deep magma storage during the 2021 La Palma eruption". *Science Advances* 9(6). DOI: 10.1126/sciadv.ade7641.

De Angelis, S. H., J. F. Larsen, M. L. Coombs, J. E. P. Utley, and A. Dunn (2020). "Phase equilibrium of a high-SiO2 andesite at f_{O_2} = RRO: implications for Augustine Volcano and other high-f_{O_2} arc andesites". *Contributions to Mineralogy and Petrology* 175(3). DOI: 10.1007/s00410-020-1663-6.

Donovan, J. J. and T. N. Tingle (1996). "An Improved Mean Atomic Number Background Correction for Quantitative Microanalysis". *Microscopy and Microanalysis* 2(1), pages 1–7. DOI: 10.1017/s1431927696210013.

Erdmann, S., B. Scaillet, C. Martel, and A. Cadoux (2014). "Characteristic Textures of Recrystallized, Peritectic, and Primary Magmatic Olivine in Experimental Samples and Natural Volcanic Rocks". *Journal of Petrology* 55(12), pages 2377–2402. DOI: 10.1093/petrology/egu060.

Fedotov, S. A., N. A. Zharinov, and L. I. Gontovaya (2010). "The magmatic system of the Klyuchevskaya group of volcanoes inferred from data on its eruptions, earthquakes, deformation, and deep structure". *Journal of Volcanol-*

ogy and Seismology 4(1), pages 1–33. DOI: 10.1134/s074204631001001x.

Feig, S. T., J. Koepke, and J. E. Snow (2010). "Effect of oxygen fugacity and water on phase equilibria of a hydrous tholeiitic basalt". *Contributions to Mineralogy and Petrology* 160(4), pages 551–568. DOI: 10.1007/s00410-010-0493-3.

Ferlito, C. (2011). "Bimodal geochemical evolution at Sheveluch stratovolcano, Kamchatka, Russia: Consequence of a complex subduction at the junction of the Kuril Kamchatka and Aleutian island arcs". *Earth-Science Reviews* 105(1-2), pages 49–69. DOI: 10.1016/j.earscirev.2010.12.003.

Freise, M., F. Holtz, M. Nowak, J. S. Scoates, and H. Strauss (2009). "Differentiation and crystallization conditions of basalts from the Kerguelen large igneous province: an experimental study". *Contributions to Mineralogy and Petrology* 158(4), pages 505–527. DOI: 10.1007/s00410-009-0394-5.

Gavrilenko, M., C. Herzberg, C. Vidito, M. J. Carr, T. Tenner, and A. Ozerov (2016). "A Calcium-in-Olivine Geohygrometer and its Application to Subduction Zone Magmatism". *Journal of Petrology* 57(9), pages 1811–1832. DOI: 10.1093/petrology/egw062.

Gavrilenko, M., M. Krawczynski, P. Ruprecht, W. Li, and J. G. Catalano (2019). "The quench control of water estimates in convergent margin magmas". *American Mineralogist* 104(7), pages 936–948. DOI: 10.2138/am-2019-6735.

Glazner, A. F. (2021). "Thermal Constraints on the Longevity, Depth, and Vertical Extent of Magmatic Systems". *Geochemistry, Geophysics, Geosystems* 22(4). DOI: 10.1029/2020gc009459.

Global Volcanism Program (2025). *Volcanoes of the World, v.5.2.4*. Edited by E. Venzke. DOI: 10.5479/si.GVP.VOTW5-2025.5.3.

Goltz, A. E. (2026). "aegoltz/Goltz-and-Krawczynski-Supplementary-Data: Release of Goltz and Krawczynski (2026) Supplementary Data". *Zenodo*. DOI: 10.5281/ZENODO.21775680. [Dataset].

Goltz, A. E., M. J. Krawczynski, M. Gavrilenko, N. V. Gorbach, and P. Ruprecht (2020). "Evidence for superhydrous primitive arc magmas from mafic enclaves at Shiveluch volcano, Kamchatka". *Contributions to Mineralogy and Petrology* 175(12). DOI: 10.1007/s00410-020-01746-5.

Goltz, A. E., M. J. Krawczynski, M. C. McCanta, and M. D. Dyar (2022). "Experimental calibration of an Fe3+/Fe2+-in-amphibole oxybarometer and its application to shallow magmatic processes at Shiveluch Volcano, Kamchatka". *American Mineralogist* 107(11), pages 2084–2100. DOI: 10.2138/am-2022-8031.

Gorbach, N. V. and M. V. Portnyagin (2011). "Geology and petrology of the lava complex of Young Shiveluch Volcano, Kamchatka". *Petrology* 19(2), pages 134–166. DOI: 10.1134/s0869591111020068.

Grove, T. L., J. M. Donnelly-Nolan, and T. Housh (1997). "Magmatic processes that generated the rhyolite of Glass Mountain, Medicine Lake volcano, N. California". *Contributions to Mineralogy and Petrology* 127(3), pages 205–223. DOI: 10.1007/s004100050276.

Grove, T. L., L. T. Elkins-Tanton, S. W. Parman, N. Chatterjee, O. Müntener, and G. A. Gaetani (2003). "Fractional crystallization and mantle-melting controls on calc-alkaline differentiation trends". *Contributions to Mineralogy and Petrology* 145(5), pages 515–533. DOI: 10.1007/s00410-003-0448-z.

Gualda, G. A. R., M. S. Ghiorso, R. V. Lemons, and T. L. Carley (2012). "Rhyolite-MELTS: a Modified Calibration of MELTS Optimized for Silica-rich, Fluid-bearing Magmatic Systems". *Journal of Petrology* 53(5), pages 875–890. DOI: 10.1093/petrology/egr080.

Hammer, J. E., M. J. Rutherford, and W. Hildreth (2002). "Magma storage prior to the 1912 eruption at Novarupta, Alaska". *Contributions to Mineralogy and Petrology* 144(2), pages 144–162. DOI: 10.1007/s00410-002-0393-2.

Harmon, L. J., G. A. Gualda, D. M. Gravley, S. L. Smithies, and C. D. Deering (2024). "The Whakamaru magmatic system (Taupō Volcanic Zone, New Zealand), part 1: Evidence from tephra deposits for the eruption of multiple magma types through time". *Journal of Volcanology and Geothermal Research* 445, page 107966. DOI: 10.1016/j.jvolgeores.2023.107966.

Hawthorne, F. C. and R. Oberti (2007). "1. Amphiboles: Crystal Chemistry". *Amphiboles*. De Gruyter, pages 1–54. ISBN: 9781501508523. DOI: 10.1515/9781501508523-002.

Helz, R. T. (1976). "Phase Relations of Basalts in their Melting Ranges at PH_2O = 5 kb. Part II. Melt Compositions". *Journal of Petrology* 17(2), pages 139–193. DOI: 10.1093/petrology/17.2.139.

Hochstaedter, A. G., P. Kepezhinskas, M. Defant, M. Drummond, and A. Koloskov (1996). "Insights into the volcanic arc mantle wedge from magnesian lavas from the Kamchatka arc". *Journal of Geophysical Research: Solid Earth* 101(B1), pages 697–712. DOI: 10.1029/95jb02404.

Holloway, J. R. and C. W. Burnham (1972). "Melting Relations of Basalt with Equilibrium Water Pressure Less Than Total Pressure". *Journal of Petrology* 13(1), pages 1–29. DOI: 10.1093/petrology/13.1.1.

Holtz, F., H. Sato, J. Lewis, H. Behrens, and S. Nakada (2005). "Experimental Petrology of the 1991-1995 Unzen Dacite, Japan. Part I: Phase Relations, Phase Composition and Pre-eruptive Conditions". *Journal of Petrology* 46(2), pages 319–337. DOI: 10.1093/petrology/egh077.

Ishikawa, T., F. Tera, and T. Nakazawa (2001). "Boron isotope and trace element systematics of the three volcanic zones in the Kamchatka arc". *Geochimica et Cosmochimica Acta* 65(24), pages 4523–4537. DOI: 10.1016/s0016-7037(01)00765-7.

Karakas, O., W. Degruyter, O. Bachmann, and J. Dufek (2017). "Lifetime and size of shallow magma bodies controlled by crustal-scale magmatism". *Nature Geoscience* 10(6), pages 446–450. DOI: 10.1038/ngeo2959.

Kawamoto, T. (1996). "Experimental constraints on differentiation and H_2O abundance of calc-alkaline magmas". *Earth and Planetary Science Letters* 144(3-4), pages 577–589. DOI: 10.1016/s0012-821x(96)00182-3.

Kelemen, P. B., D. B. Joyce, J. D. Webster, and J. R. Holloway (1990). "Reaction Between Ultramafic Rock and Fractionating Basaltic Magma II. Experimental Investigation of Reaction Between Olivine Tholeiite and Harzburgite at 1150-1050 C and 5 kb". *Journal of Petrology* 31(1), pages 99–134. DOI: 10.1093/petrology/31.1.99.

King, P., R. Hervig, J. Holloway, J. Delaney, and M. Dyar (2000). "Partitioning of Fe3+/Fetotal between amphibole and basanitic melt as a function of oxygen fugacity". *Earth and Planetary Science Letters* 178(1-2), pages 97–112. DOI: 10.1016/s0012-821x(00)00071-6.

King, P., R. Hervig, J. Holloway, T. Vennemann, and K. Righter (1999). "Oxy-substitution and dehydrogenation in mantle-derived amphibole megacrysts". *Geochimica et Cosmochimica Acta* 63(21), pages 3635–3651. DOI: 10.1016/s0016-7037(99)00162-3.

Koch, L., R. R. Almeev, S. A. Linsler, F. Marxer, and F. Holtz (2025). "The effect of H_2O on the crystallization of orthopyroxene in a high-Mg andesitic melt". *American Mineralogist* 110(12). Edited by Y. Morizet, pages 2007–2016. DOI: 10.2138/am-2024-9593.

Krawczynski, M. J. (2011). "Experimental studies of melting and crystallization processes in planetary interiors". Ph.D. Thesis. Massachusetts Institute of Technology and Woods Hole Oceanographic Institution. DOI: 10.1575/1912/4837.

Krawczynski, M. J., T. L. Grove, and H. Behrens (2012). "Amphibole stability in primitive arc magmas: effects of temperature, H_2O content, and oxygen fugacity". *Contributions to Mineralogy and Petrology* 164(2), pages 317–339. DOI: 10.1007/s00410-012-0740-x.

Larocque, J. and D. Canil (2010). "The role of amphibole in the evolution of arc magmas and crust: the case from the Jurassic Bonanza arc section, Vancouver Island, Canada". *Contributions to Mineralogy and Petrology* 159(4), pages 475–492. DOI: 10.1007/s00410-009-0436-z.

Mandler, B. E. and T. L. Grove (2016). "Controls on the stability and composition of amphibole in the Earth's mantle". *Contributions to Mineralogy and Petrology* 171(8-9). DOI: 10.1007/s00410-016-1281-5.

Martel, C., M. Pichavant, F. Holtz, B. Scaillet, J.-L. Bourdier, and H. Traineau (1999). "Effects of f_{O_2} and H_2O on andesite phase relations between 2 and 4 kbar". *Journal of Geophysical Research: Solid Earth* 104(B12), pages 29453–29470. DOI: 10.1029/1999jb900191.

Marxer, F., P. Ulmer, and O. Müntener (2022). "Polybaric fractional crystallisation of arc magmas: an experimental study simulating trans-crustal magmatic systems". *Contributions to Mineralogy and Petrology* 177(1). DOI: 10.1007/s00410-021-01856-8.

– (2023). "Ascent-driven differentiation: a mechanism to keep arc magmas metaluminous?" *Contributions to Mineralogy and Petrology* 178(8). DOI: 10.1007/s00410-023-02035-7.

Masotta, M., A. Pontesilli, S. Mollo, P. Armienti, T. Ubide, M. Nazzari, and P. Scarlato (2020). "The role of undercooling during clinopyroxene growth in trachybasaltic magmas: Insights on magma decompression and cooling at Mt. Etna volcano". *Geochimica et Cosmochimica Acta* 268, pages 258–276. DOI: 10.1016/j.gca.2019.10.009.

Matjuschkin, V., R. A. Brooker, B. Tattitch, J. D. Blundy, and C. C. Stamper (2015). "Control and monitoring of oxygen fugacity in piston cylinder experiments". *Contributions to Mineralogy and Petrology* 169(1). DOI: 10.1007/s00410-015-1105-z.

McCanta, M. C., M. J. Rutherford, and J. E. Hammer (2007). "Pre-eruptive and syn-eruptive conditions in the Black Butte, California dacite: Insight into crystallization kinetics in a silicic magma system". *Journal of Volcanology and Geothermal Research* 160(3-4), pages 263–284. DOI: 10.1016/j.jvolgeores.2006.10.004.

Melekhova, E., J. Blundy, R. Robertson, and M. C. S. Humphreys (2015). "Experimental Evidence for Polybaric Differentiation of Primitive Arc Basalt beneath St. Vincent, Lesser Antilles". *Journal of Petrology* 56(1), pages 161–192. DOI: 10.1093/petrology/egu074.

Mitchell, A. L., G. A. Gaetani, J. A. O'Leary, and E. H. Hauri (2017). "H_2O solubility in basalt at upper mantle conditions". *Contributions to Mineralogy and Petrology* 172(10). DOI: 10.1007/s00410-017-1401-x.

Moore, G. and I. S. E. Carmichael (1998). "The hydrous phase equilibria (to 3 kbar) of an andesite and basaltic andesite from western Mexico: constraints on water content and conditions of phenocryst growth". *Contributions to Mineralogy and Petrology* 130(3-4), pages 304–319. DOI: 10.1007/s004100050367.

Müntener, O., P. B. Kelemen, and T. L. Grove (2001). "The role of H_2O during crystallization of primitive arc magmas under uppermost mantle conditions and genesis of igneous pyroxenites: an experimental study". *Contributions to Mineralogy and Petrology* 141(6), pages 643–658. DOI: 10.1007/s004100100266.

Nandedkar, R. H., N. Hürlimann, P. Ulmer, and O. Müntener (2016). "Amphibole–melt trace element partitioning of fractionating calc-alkaline magmas in the lower crust: an experimental study". *Contributions to Mineralogy and Petrology* 171(8-9). DOI: 10.1007/s00410-016-1278-0.

Nandedkar, R. H., P. Ulmer, and O. Müntener (2014). "Fractional crystallization of primitive, hydrous arc magmas: an experimental study at 0.7 GPa". *Contributions to Mineralogy and Petrology* 167(6). DOI: 10.1007/s00410-014-1015-5.

Oberti, R., F. C. Hawthorne, E. Cannillo, and F. Camara (2007). "Long-Range Order in Amphiboles". *Reviews in Mineralogy and Geochemistry* 67(1), pages 125–171. DOI: 10.2138/rmg.2007.67.4.

Pamukcu, A. S., G. A. R. Gualda, M. S. Ghiorso, C. F. Miller, and R. G. McCracken (2015). "Phase-equilibrium geobarometers for silicic rocks based on rhyolite-MELTS—Part 3: Application to the Peach Spring Tuff (Arizona–California–Nevada, USA)". *Contributions to Mineralogy and Petrology* 169(3). DOI: 10.1007/s00410-015-1122-y.

Pichavant, M., S. Poussineau, P. Lesne, C. Solaro, and J. .-. Bourdier (2018). "Experimental Parametrization of Magma Mixing: Application to the ad 1530 Eruption of La Soufrière, Guadeloupe (Lesser Antilles)". *Journal of Petrology* 59(2), pages 257–282. DOI: 10.1093/petrology/egy030.

Pichavant, M., C. Martel, J.-L. Bourdier, and B. Scaillet (2002). "Physical conditions, structure, and dynamics of a zoned magma chamber: Mount Pelée (Martinique, Lesser Antilles Arc)". *Journal of Geophysical Research: Solid Earth* 107(B5). DOI: 10.1029/2001jb000315.

Ponomareva, V., I. Melekestsev, O. Braitseva, T. Churikova, M. Pevzner, and L. Sulerzhitsky (2007). "Late Pleistocene-Holocene volcanism on the Kamchatka Peninsula, Northwest Pacific Region". *Volcanism and Subduction: The Kamchatka Region*. American Geophysical Union, pages 165–198. ISBN: 9780875904368. DOI: 10.1029/172gm15.

Ponomareva, V., M. Portnyagin, M. Pevzner, M. Blaauw, P. Kyle, and A. Derkachev (2015). "Tephra from andesitic Shiveluch volcano, Kamchatka, NW Pacific: chronology of explosive eruptions and geochemical fingerprinting of volcanic glass". *International Journal of Earth Sciences* 104(5), pages 1459–1482. DOI: 10.1007/s00531-015-1156-4.

Prissel, K., J.-A. Olive, and M. J. Krawczynski (2023). "A Log-Ratio-Based Algorithm for Petrologic Mass-Balance Problems and Uncertainty Assessment". *Geochemistry, Geophysics, Geosystems* 24(12). DOI: 10.1029/2023gc011234.

Prouteau, G. and B. Scaillet (2003). "Experimental Constraints on the Origin of the 1991 Pinatubo Dacite". *Journal of Petrology* 44(12), pages 2203–2241. DOI: 10.1093/petrology/egg075.

Prouteau, G., B. Scaillet, M. Pichavant, and R. C. Maury (1999). "Fluid-present melting of ocean crust in subduction zones". *Geology* 27(12), page 1111. DOI: 10.1130/0091-7613(1999)027<1111:fpmooc>2.3.co;2.

Prouteau, G., B. Scaillet, M. Pichavant, and R. Maury (2001). "Evidence for mantle metasomatism by hydrous silicic melts derived from subducted oceanic crust". *Nature* 410(6825), pages 197–200. DOI: 10.1038/35065583.

Putak Juriček, M. and H. Keppler (2023). "Amphibole stability, water storage in the mantle, and the nature of the lithosphere-asthenosphere boundary". *Earth and Planetary Science Letters* 608, page 118082. DOI: 10.1016/j.epsl.2023.118082.

Putirka, K. D. (2008). "Thermometers and Barometers for Volcanic Systems". *Reviews in Mineralogy and Geochemistry* 69(1), pages 61–120. DOI: 10.2138/rmg.2008.69.3.

Putirka, K. (2016). "Amphibole thermometers and barometers for igneous systems and some implications for eruption mechanisms of felsic magmas at arc volcanoes". *American Mineralogist* 101(4), pages 841–858. DOI: 10.2138/am-2016-5506.

Rezeau, H., B. Z. Klein, and O. Jagoutz (2021). "Mixing dry and wet magmas in the lower crust of a continental arc: new petrological insights from the Bear Valley Intrusive Suite, southern Sierra Nevada, California". *Contributions to Mineralogy and Petrology* 176(9). DOI: 10.1007/s00410-021-01832-2.

Ridolfi, F., A. Renzulli, and M. Puerini (2010). "Stability and chemical equilibrium of amphibole in calc-alkaline magmas: an overview, new thermobarometric formulations and application to subduction-related volcanoes". *Contributions to Mineralogy and Petrology* 160(1), pages 45–66. DOI: 10.1007/s00410-009-0465-7.

Roeder, P. L. and R. F. Emslie (1970). "Olivine-liquid equilibrium". *Contributions to Mineralogy and Petrology* 29(4), pages 275–289. DOI: 10.1007/bf00371276.

Ruprecht, P., A. C. Simon, and A. Fiege (2020). "The Survival of Mafic Magmatic Enclaves and the Timing of Magma Recharge". *Geophysical Research Letters* 47(14). DOI: 10.1029/2020gl087186.

Rutherford, M. J. (2003). "Magmatic Conditions and Magma Ascent as Indicated by Hornblende Phase Equilibria and Reactions in the 1995-2002 Soufriere Hills Magma". *Journal of Petrology* 44(8), pages 1433–1453. DOI: 10.1093/petrology/44.8.1433.

Rutherford, M. J. and J. D. Devine (1996). "Preeruption pressure-temperature conditions and volatiles in the 1991 dacitic magma of Mount Pinatubo". *Fire and Mud: Eruptions and Lahars of Mount Pinatubo, Philippines*. Edited by C. Newhall and S. Raymundo. University of Washington Press, pages 751–766. ISBN: 9780295975856.

Rutherford, M. J., H. Sigurdsson, S. Carey, and A. Davis (1985). "The May 18, 1980, eruption of Mount St. Helens: 1. Melt composition and experimental phase equilibria". *Journal of Geophysical Research: Solid Earth* 90(B4), pages 2929–2947. DOI: 10.1029/jb090ib04p02929.

Rutherford, M. J. and J. D. Devine (1988). "The May 18, 1980, eruption of Mount St. Helens: 3. Stability and chemistry of amphibole in the magma chamber". *Journal of Geophysical Research: Solid Earth* 93(B10), pages 11949–11959. DOI: 10.1029/jb093ib10p11949.

Scaillet, B. and B. W. Evans (1999). "The 15 June 1991 Eruption of Mount Pinatubo. I. Phase Equilibria and Pre-eruption P-T-f_{O_2}-f_{H_2O} Conditions of the Dacite Magma". *Journal of Petrology* 40(3), pages 381–411. DOI: 10.1093/petroj/40.3.381.

Shea, T. and J. E. Hammer (2013). "Kinetics of cooling- and decompression-induced crystallization in hydrous mafic-intermediate magmas". *Journal of Volcanology and Geothermal Research* 260, pages 127–145. DOI: 10.1016/j.jvolgeores.2013.04.018.

Sisson, T. W. and T. L. Grove (1993). "Experimental investigations of the role of H_2O in calc-alkaline differentiation and subduction zone magmatism". *Contributions to Mineralogy and Petrology* 113(2), pages 143–166. DOI: 10.1007/bf00283225.

Sisson, T. W., K. Ratajeski, W. B. Hankins, and A. F. Glazner (2005). "Voluminous granitic magmas from common basaltic sources". *Contributions to Mineralogy and Petrology* 148(6), pages 635–661. DOI: 10.1007/s00410-004-0632-9.

Till, C. B., A. J. R. Kent, G. A. Abers, H. A. Janiszewski, J. B. Gaherty, and B. W. Pitcher (2019). "The causes of spatiotemporal variations in erupted fluxes and compositions along a volcanic arc". *Nature Communications* 10(1). DOI: 10.1038/s41467-019-09113-0.

Ulmer, P., R. Kaegi, and O. Müntener (2018). "Experimentally Derived Intermediate to Silica-rich Arc Magmas by Fractional and Equilibrium Crystallization at 1·0 GPa: an Evalu-

ation of Phase Relationships, Compositions, Liquid Lines of Descent and Oxygen Fugacity". *Journal of Petrology* 59(1), pages 11–58. DOI: 10.1093/petrology/egy017.

Volynets, O. N., V. v. Ponomareva, and A. D. Babansky (1997). "Magnesian basalts of Shiveluch andesite volcano, Kamchatka". *Petrologiya* 5 (2), pages 206–221.

Wallace, M. and D. H. Green (1991). "The effect of bulk rock composition on the stability of amphibole in the upper mantle: Implications for solidus positions and mantle metasomatism". *Mineralogy and Petrology* 44(1-2), pages 1–19. DOI: 10.1007/bf01167097.

Waters, L. E., E. Cottrell, M. L. Coombs, and K. A. Kelley (2021). "Generation of Calc-Alkaline Magmas during Crystallization at High Oxygen Fugacity: An Experimental and Petrologic Study of Tephras from Buldir Volcano, Western Aleutian Arc, Alaska, USA". *Journal of Petrology* 62(3). DOI: 10.1093/petrology/egaa104.

Weber, G. and J. Blundy (2024). "A Machine Learning-Based Thermobarometer for Magmatic Liquids". *Journal of Petrology* 65(4). DOI: 10.1093/petrology/egae020.

Welsch, B., F. Faure, V. Famin, A. Baronnet, and P. Bachèlery (2013). "Dendritic Crystallization: A Single Process for all the Textures of Olivine in Basalts?" *Journal of Petrology* 54(3), pages 539–574. DOI: 10.1093/petrology/egs077.

Wieser, P., M. Petrelli, J. Lubbers, E. Wieser, S. Ozaydin, A. Kent, and C. Till (2022). "Thermobar: An open-source Python3 tool for thermobarometry and hygrometry". *Volcanica* 5(2), pages 349–384. DOI: 10.30909/vol.05.02.349384.

Wieser, P. E., A. J. R. Kent, C. B. Till, and G. A. Abers (2023). "Geophysical and Geochemical Constraints on Magma Storage Depths Along the Cascade Arc: Knowns and Unknowns". *Geochemistry, Geophysics, Geosystems* 24(11). DOI: 10.1029/2023gc011025.

Yoder, H. S. and C. E. Tilley (1962). "Origin of Basalt Magmas: An Experimental Study of Natural and Synthetic Rock Systems". *Journal of Petrology* 3(3), pages 342–532. DOI: 10.1093/petrology/3.3.342.